Adaptive Mode Control in Few-Mode and Highly Multimode Fibers

Tong Qiu

Thesis submitted to the faculty of the Virginia Polytechnic Institute and State University in partial fulfillment of the requirements for the degree of

Master of Science

In

Electrical Engineering

Yong Xu

Anbo Wang

Yizheng Zhu

12/06/2017

Blacksburg, VA

Keywords: Adaptive Optics, fiber optics, few-mode fibers, multimode fibers, mode control, mode division multiplexing, fiber Bragg gratings

Adaptive Mode Control in Few-Mode and Highly Multimode Fibers

Tong Qiu

Abstract

Few-mode fibers (FMFs) and multimode fibers (MMFs) can provide much higher data-carrying capacities compared with single-mode fibers. But in order to achieve this goal, one must address the challenge of intermodal coupling and dispersion. Therefore the ability to accurately control the optical signal propagation in FMFs/MMFs can play a pivotal role in FMF/MMF applications. This thesis demonstrates the ability to excite, in FMFs and MMFs, the desired linearly polarized (LP) modes as well as their superpositions through adaptive optics (AO). Specifically, in the case of step-index FMFs, a phase-only spatial light modulator (SLM) is employed to manipulate the light at the fiber input end, driven by the feedback signal provided by the correlation between the charge coupled device (CCD) camera captured images at the fiber output end and the target light intensity profile. Through such an adaptive optical system, any arbitrarily selected LP modes can be excited at the distal end of the four-mode and seventeen-mode fibers, respectively. For a graded-index MMF with a uniform Bragg grating, we use a deformable mirror (DM) to perform the wavefront modulation at the fiber input end, where the feedback is based on the ratio of the grating-reflected signal power to the transmitted signal power. At the Bragg grating position of this highly multimode fiber, any desired principal mode groups can be successfully chosen. These experimental results suggest that adaptive control of optical wavefront in FMFs/MMFs is indeed feasible.

Adaptive Mode Control in Few-Mode and Highly Multimode Fibers

Tong Qiu

General Audience Abstract

Optical fibers, in terms of the number of modes they support, can be generally divided into single-mode fibers (SMFs), and few-mode fibers/multimode fibers (FMFs/MMFs). FMFs/MMFs can provide much higher data-carrying capacities than SMFs. For example, an FMF/MMF that supports M modes can ideally increase the data transmission rate by a factor of M, where each mode can serve as a distinct communication channel. However, in order to achieve good performance, one must accurately control signal propagation in FMFs/MMFs, which are often degraded due to the multiple-mode nature. This thesis demonstrates the ability, using adaptive optics (AO), to control signal propagation in FMFs and a highly MMF, respectively. Specifically, in the case of FMFs, a phase-only spatial light modulator (SLM) is employed to manipulate the light at the fiber input, driven by AO feedback signal provided by the similarity between the real-time fiber output image and the target mode profile. Through such an adaptive optical system, any desired linearly-polarized (LP) modes can be excited at the output of the four-mode and seventeen-mode fibers, respectively. For the highly MMF with uniform Bragg grating, we use a deformable mirror (DM) to perform the wavefront modulation at the fiber input, where AO feedback is provided by the fiber Bragg grating (FBG) reflectivity. At the FBG position, any desired principal mode groups can be successfully chosen. These experimental results suggest that adaptive control of optical wavefront in FMFs/MMFs is indeed feasible, and may find a large number of applications in optical communication, sensing, and imaging.

Acknowledgement

Foremost, I would like to express my sincere gratitude to my advisor Dr. Yong Xu, who provides me with a free but instructive environment to pursue my degree. It would be such an honor to be his student, for the example he set as an excellent researcher, for the support he provided for my degree pursuit, for the brilliant ideas and inspirations he shared, and so on so forth.

Besides my advisor, my sincere thanks also goes to the rest of my thesis committee: Dr. Anbo Wang and Dr. Yizheng Zhu. I appreciate Dr. Wang for offering me help and opportunities when I was in urgent need, and for providing the full access to his lab facilities. I also thank Dr. Zhu for the helpful discussions on either my research or lectures.

Further gratitude is for Dr. Islam Ashry, Dr. Peng Lu and all of my colleagues, for their suggestions and help.

Last but not the least, I would like to thank my friends and my family, because of their supports, accompanies, and encouragements, I became what I am today.

Contents

List of abbreviations

AO	Adaptive optics
DM	Deformable mirror
FBG	Fiber Bragg grating
FMF	Few-mode fiber
LP	Linearly polarized
MDM	Mode-division multiplexing
MMF	Multimode fiber
MIMO	Multiple-input-multiple-output
NLC	Nematic liquid crystal
RI	Refractive index
SLM	Spatial light modulator
SMF	Single-mode fiber
TM	Transfer matrix
TMF	Two-mode fiber

Chapter 1

Introduction

Optical fibers, characterized by lightweight, high flexibility, small size, etc. have become one of the most attractive components in numerous areas. Traditionally, single-mode fibers (SMFs) are usually the preferred platform for practical applications, compared with few-mode fibers (FMFs) or multimode fibers (MMFs). In FMFs/MMFs, the optical signals tend to experience far more significant intermodal dispersion arising from the multimode nature [1], together with the inevitable modal chaos introduced by imperfect fabrication, fiber bending, stress, etc. [2]. These two factors twist together and can render the FMF/MMF an unreliable signal transmission channel. However, with the continued growth of data traffic, the limited transmission capacity of SMFs is unlikely to support our information-driven society [3]. To move beyond such limitations of SMFs, researchers have studied multiplexing in time, wavelength, and polarization domain for decades [4-6]. Yet three dimensions of single fibers have been explored to increase data-carrying capacity, whereas the spatial dimension remains untapped. However, this new dimension starts to play a role recently, with the development of mode-division multiplexing (MDM).

1.1 Mode-Division Multiplexing

The concept of MDM was proposed as far back as 1982 [7], the principle is quite straightforward: In an MDM system with M modes, if one can utilize these entire modes as M distinct transmission channels, the overall transmission capacity of the fiber network could increase by a factor of M. However, subject to technology limitations, the implementations of MDM in telecommunications were delayed until the emergence of optical multiple-input-multiple-out (MIMO) digital signal processing technique. MIMO technique was originally developed for wireless microwave communications [8], where antenna array elements serve as transmitters and receivers, and the radio signals propagate in a rich scattering environment. The scattering environment is an analogy to FMFs/MMFs where the optical signals propagate as fiber modes. In FMFs/MMFs, the presence of intermodal coupling and differential mode group delay can randomize the light propagation and thus make the signals indeterminable at the receiver end [9]. To recover the signals at the receivers, MIMO technique needs to be performed: One can determine the transfer function of the system by sending training symbols [1]. Some successful realizations of MDM strategy are elaborated in [10-12]. In addition to optical communications, the concept of MDM can also be extended to sensing [13], imaging [14, 15], and micromanipulation [16] to name just a few.

However, for all those applications, one major challenge is how to accurately control the optical signals in real-life fibers, *i.e.* in the presence of random coupling and dispersion. Such issues can be settled by multiple techniques, among which long period gratings in MMFs [17], spot-based samplers [18], phase masks [19, 20], and spatial light modulators (SLMs) [11, 21, 22] are primarily applied in optical communications; photonic lanterns [23, 24], endoscopes [25], and transfer matrix calibrations [26] are originally developed for imaging applications. These existing approaches can significantly improve the performance of FMFs/MMFs, whereas most of them lack of adaptability and acceptable tolerance to environmental perturbations. Aiming to address these two issues, our group have proposed and implemented a new mode selection mechanism based on adaptive optics (AO) [27-29].

1.2 Adaptive Optics

AO is a scientific and engineering discipline, which aims to improve the performance of an optical system by using information about the environment the optical signal passes [30]. Originally developed for astronomy to correct and recover an image for a higher resolution, the concept of AO has been extended to biomedical imaging since the late 1970s. Retinal *in vivo* imaging is one of the most promising application areas, where it is notoriously known that the quality of the retinal images can be prohibitively degraded by human eye aberrations (defocus, astigmatism, coma, spherical aberration, monochromatic aberration, etc.), especially when the pupil size is large [31]. Conventional ophthalmoscopy techniques, such as scanning laser ophthalmoscopy [32] and optical coherent tomography [33], suffer from those aberrations. However, the merging of the traditional ophthalmoscopy techniques and AO can considerably reduce the impacts of most aberrations and thus improve the image resolution [34-36]. Below we explain the principle behind it: The effects of ocular and system aberrations on the optical signal distortion can be adequately modeled by a wavefront distortion (or phase) $\theta(x, y)$ across the entrance pupil of the taking system [37]. If one can compensate such a distortion by introducing a $-\theta(x, y)$ phase change, an aberration-free image can be recovered in principle. Further, this conjugate phase shift $-\theta(x, y)$ can be determined and realized by an adaptive optical system. In that system, the wavefront is firstly measured by one means or another [31, 37, 38], and then a set of control signals is developed to drive a phase modulation device, so that the image blurring is mostly removed.

Beyond living human retinal imaging, AO can also be incorporated with modern microscopy technologies to observe large populations of neurons *in vivo* at single-synapse resolution [39], in which the researchers extended AO approach to strongly scattered tissues by exploiting the reduced scattering of near-infrared guide stars, and achieved a functional imaging down to 700 mm inside the mouse brain. More recently, the emergence of multi-pupil AO enables simultaneous wavefront correction over a large field of view [40], which further enables 3D nonplanar imaging *in vivo*.

Our group incorporates AO with fiber optics, where the compensation for unpredictable mode coupling and intermodal dispersion can be determined through an adaptive optical system.

1.3 Organization

This thesis is organized as follows:

Chapter 2: Background

In this chapter, we briefly introduce the background knowledge and the major devices used in this thesis. We first summarize the theoretical analysis of optical fibers, including the step-index and graded-index fibers. We then proceed to wavefront modulation, mathematically show the process of phase modulation. Then we introduce two major phase modulation devices, which are respectively based on liquid crystal and reflecting mirrors. In the subsequent section, we turn to the fiber Bragg grating, start from its fabrication to reflection characteristics, among which coupled-mode theory is briefly discussed.

Chapter 3: Adaptive Mode Control in Four- and seventeen-Mode Fibers

In this chapter, we investigate the effectiveness of applying AO to mode control in the step-index FMFs, using the feedback provided by the correlation between the experimentally captured intensity distributions and the theoretical desired mode profile. We experimentally demonstrate the ability to control the linearly polarized modes respectively in four- and seventeen-mode fibers through a phase-only spatial light modulator. Mode decomposition is then performed, and the results of selective excitations of individual fiber modes are shown.

Chapter 4: Adaptive Mode Control in Highly Multimode Fibers

In this chapter, we move from the FMFs to MMFs, using AO to selectively excite the fiber mode groups within a graded-index MMF with a uniform fiber Bragg grating inscribed towards the distal end. A deformable mirror is used to modulate the fiber input wavefront, based on the feedback signal provided by the ratio of grating-reflected signal power to the transmitted signal power. Selective excitations of the low-, intermediate-, and high-order mode groups are experimentally achieved.

Chapter 5: Conclusions

In this chapter, we draw the conclusions of our two experiments.

References

1. A. R. Shah, R. C. J. Hsu, A. Tarighat, A. H. Sayed, and B. Jalali, "Coherent optical MIMO (COMIMO)," J. Lightwave Technol. **23**, 2410-2419 (2005)
2. L. Palmieri, "Coupling mechanism in multimode fibers," Next-Generation Optical Communication: Components, Sub-Systems, and Systems Iii **9009** (2014).
3. R. J. Essiambre and R. W. Tkach, "Capacity Trends and Limits of Optical Communication Networks," Proc. IEEE **100**, 1035-1055 (2012).
4. W. R. Bennett, "Time division multiplex systems," Bell Syst. Tech. J. **20**, 199-221 (1941).
5. T. Miki and H. Ishio, "Viabilities of Wavelength-Division-Multiplexing Transmission-System over an Optical Fiber Cable," IEEE Trans. Commun. **26**, 1082-1087 (1978).

6. S. G. Evangelides, L. F. Mollenauer, J. P. Gordon, and N. S. Bergano, "Polarization Multiplexing with Solitons," J. Lightwave Technol. **10**, 28-35 (1992).

7. S. Berdague and P. Facq, "Mode Division Multiplexing in Optical Fibers," Appl. Opt. **21**, 1950-1955 (1982).

8. G. J. Foschini, "Layered space-time architecture for wireless communication in a fading environment when using multi-element antennas," Bell Syst. Tech. J. **1**, 41-59 (1996).

9. D. J. Richardson, J. M. Fini, and L. E. Nelson, "Space-division multiplexing in optical fibres," Nat. Photonics **7**, 354-362 (2013).

10. S. J. Savory, "Digital Coherent Optical Receivers: Algorithms and Subsystems," IEEE J. Sel. Topics Quantum Electron. **16**, 1164-1179 (2010).

11. M. Salsi, C. Koebele, D. Sperti, P. Tran, P. Brindel, H. Mardoyan, S. Bigo, A. Boutin, F. Verluise, P. Sillard, M. Astruc, L. Provost, F. Cerou, and G. Charlet, "Transmission at 2x100Gb/s, over Two Modes of 40km-long Prototype Few-Mode Fiber, using LCOS-based Mode Multiplexer and Demultiplexer," 2011 Optical Fiber Communication Conference and Exposition (OFC/NFOEC) and the National Fiber Optic Engineers Conference (2011).

12. N. Hanzawa, K. Saitoh, T. Sakamoto, T. Matsui, S. Tomita, and M. Koshiba, "Demonstration of mode-division multiplexing transmission over 10 km two-mode fiber with mode coupler," 2011 Optical Fiber Communication Conference and Exposition (OFC/NFOEC) and the National Fiber Optic Engineers Conference (2011).

13. E. B. Li, X. L. Wang, and C. Zhang, "Fiber-optic temperature sensor based on interference of selective higher-order modes," Appl. Phys. Lett. **89** (2006).

14. T. Cizmar and K. Dholakia, "Exploiting multimode waveguides for pure fibre-based imaging," Nat. Commun. **3** (2012).

15. Y. Choi, C. Yoon, M. Kim, T. D. Yang, C. Fang-Yen, R. R. Dasari, K. J. Lee, and W. Choi, "Scanner-Free and Wide-Field Endoscopic Imaging by Using a Single Multimode Optical Fiber," Phys. Rev. Lett. **109** (2012).

16. T. Cizmar, M. Mazilu, and K. Dholakia, "In situ wavefront correction and its application to micromanipulation," Nat. Photonics **4**, 388-394 (2010).

17. A. Li, A. Al Amin, X. Chen, and W. Shieh, "Reception of Mode and Polarization Multiplexed 107-Gb/s CO-OFDM Signal over a Two-Mode Fiber," 2011 Optical Fiber Communication

Conference and Exposition (OFC/NFOEC) and the National Fiber Optic Engineers Conference (2011).

18. R. Ryf, N. K. Fontaine, and R. J. Essiambre, "Spot-Based Mode Couplers for Mode-Multiplexed Transmission in Few-Mode Fiber," IEEE Photonics Technol. Lett. **24**, 1973-1976 (2012).
19. R. Ryf, S. Randel, A. H. Gnauck, C. Bolle, R. J. Essiambre, P. J. Winzer, D. W. Peckham, A. McCurdy, and R. Lingle, "Space-division multiplexing over 10 km of three-mode fiber using coherent 6 x 6 MIMO processing," 2011 Optical Fiber Communication Conference and Exposition (OFC/NFOEC) and the National Fiber Optic Engineers Conference (2011).
20. N. Bai, E. Ip, Y. K. Huang, E. Mateo, F. Yaman, M. J. Li, S. Bickham, S. Ten, J. Linares, C. Montero, V. Moreno, X. Prieto, V. Tse, K. M. Chung, A. P. T. Lau, H. Y. Tam, C. Lu, Y. H. Luo, G. D. Peng, G. F. Li, and T. Wang, "Mode-division multiplexed transmission with inline few-mode fiber amplifier," Opt. Express **20**, 2668-2680 (2012).
21. J. Carpenter and T. D. Wilkinson, "All Optical Mode-Multiplexing Using Holography and Multimode Fiber Couplers," J. Lightwave Technol. **30**, 1978-1984 (2012).
22. J. von Hoyningen-Huene, R. Ryf, and P. Winzer, "LCoS-based mode shaper for few-mode fiber," Opt. Express **21**, 18097-18110 (2013).
23. S. G. Leon-Saval, A. Argyros, and J. Bland-Hawthorn, "Photonic lanterns: a study of light propagation in multimode to single-mode converters," Opt. Express **18**, 8430-8439 (2010).
24. N. K. Fontaine, R. R. Ryf, S. G. Leon-Saval, and J. Bland-Hawthorn, "Evaluation of Photonic Lanterns for Lossless Mode-Multiplexing," 2012 38th European Conference and Exhibition on Optical Communications (ECOC) (2012).
25. K. L. Reichenbach and C. Xu, "Numerical analysis of light propagation in image fibers or coherent fiber bundles," Opt. Express **15**, 2151-2165 (2007).
26. M. Ploschner, T. Tyc, and T. Cizmar, "Seeing through chaos in multimode fibres," Nat. Photonics **9**, 529-+ (2015).
27. P. Lu, M. Shipton, A. B. Wang, S. Soker, and Y. Xu, "Adaptive control of waveguide modes in a two-mode-fiber," Opt. Express **22**, 2955-2964 (2014).
28. P. Lu, M. Shipton, A. B. Wang, and Y. Xu, "Adaptive control of waveguide modes using a directional coupler," Opt. Express **22**, 20000-20007 (2014).

29. P. Lu, A. B. Wang, S. Soker, and Y. Xu, "Adaptive mode control based on a fiber Bragg grating," Opt. Lett. **40**, 3488-3491 (2015).
30. R. K. Tyson, “Principles of adaptive optics,” CRC press (2015).
31. J. Z. Liang and D. R. Williams, "Aberrations and retinal image quality of the normal human eye," J. Opt. Soc. Am. A **14**, 2873-2883 (1997).
32. R. H. Webb, G. W. Hughes, and F. C. Delori, "Confocal Scanning Laser Ophthalmoscope," Appl. Opt. **26**, 1492-1499 (1987).
33. D. Huang, E. A. Swanson, C. P. Lin, J. S. Schuman, W. G. Stinson, W. Chang, M. R. Hee, T. Flotte, K. Gregory, C. A. Puliafito, and J. G. Fujimoto, "Optical Coherence Tomography," Science **254**, 1178-1181 (1991).
34. A. Roorda, F. Romero-Borja, W. J. Donnelly, H. Queener, T. J. Hebert, and M. C. W. Campbell, "Adaptive optics scanning laser ophthalmoscopy," Optics Express **10**, 405-412 (2002).
35. B. Hermann, E. J. Fernandez, A. Unterhuber, H. Sattmann, A. F. Fercher, W. Drexler, P. M. Prieto, and P. Artal, "Adaptive-optics ultrahigh-resolution optical coherence tomography," Opt Lett **29**, 2142-2144 (2004).
36. R. J. Zawadzki, S. M. Jones, S. S. Olivier, M. T. Zhao, B. A. Bower, J. A. Izatt, S. Choi, S. Laut, and J. S. Werner, "Adaptive-optics optical coherence tomography for high-resolution and high-speed 3D retinal in vivo imaging," Opt. Express **13**, 8532-8546 (2005).
37. R. A. Gonsalves, "Phase Retrieval and Diversity in Adaptive Optics," Opt. Eng. **21**, 829-832 (1982).
38. F. Roddier, "Curvature Sensing and Compensation - a New Concept in Adaptive Optics," Appl. Opt. **27**, 1223-1225 (1988).
39. K. Wang, W. Z. Sun, C. T. Richie, B. K. Harvey, E. Betzig, and N. Ji, "Direct wavefront sensing for high-resolution in vivo imaging in scattering tissue," Nat. Commun. **6** (2015).
40. J. H. Park, L. J. Kong, Y. F. Zhou, and M. Cui, "Large-field-of-view imaging by multi-pupil adaptive optics," Nat. Methods **14**, 581-+ (2017).

Chapter 2

Background

2.1 Optical Fibers

Optical fibers are cylindrical dielectric waveguides with higher refractive index (RI) in the middle and lower RI surrounded. Figure 2.1 shows the typical geometric structure of a step-index fiber and its corresponding RI distribution along radius.

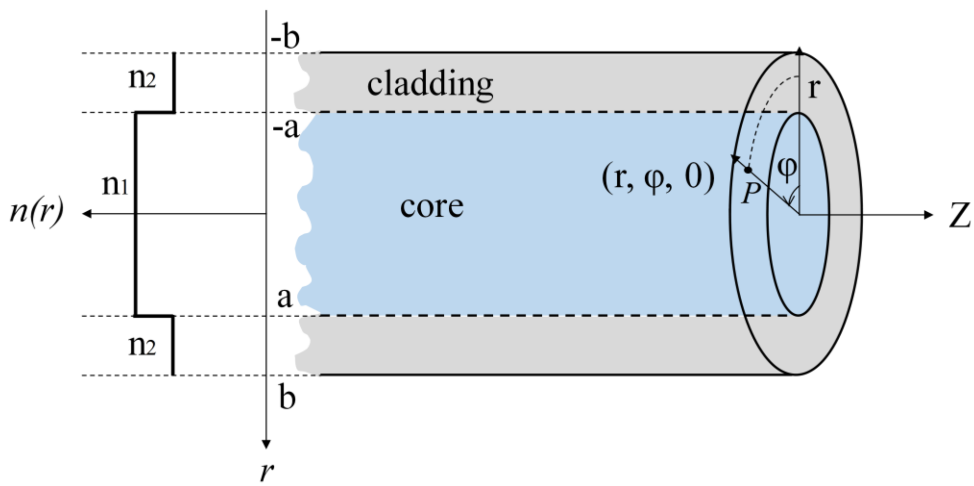

Fig. 2.1. Representative geometric structure of a step-index fiber in cylindrical coordinates, and its index distribution *n(r)* along radius. The core region and cladding region are in blue and grey, with index values as n_1 and n_2 , and radius values as a and b, respectively. An observation point *P* (r, φ, 0) is placed in the plane $Z = 0$.

One can summarize the RI distribution on cross-section of step-index fibers as below:

$$n(r) = \begin{cases} n_1, & |r| \le a \\ n_2, & |r| > a \end{cases}. \qquad 2.1$$

2.1.1 Step-Index Fibers and Linearly-Polarized Modes

In linear, source-free, isotropic dielectric media, the four Maxwell's equations can be simplified as:

$$\nabla^2 \mathbf{E} = \varepsilon\mu \frac{\partial^2 \mathbf{E}}{\partial t^2}, \tag{2.2a}$$

$$\nabla^2 \mathbf{H} = \varepsilon\mu \frac{\partial^2 \mathbf{H}}{\partial t^2}, \tag{2.2b}$$

where ε and μ are the permittivity and permeability of the media in which the light is propagating. Equations. 2.2a and 2.2b are the standard *wave equations*.

Consider the case where the light is propagating along a step-index fiber shown in Fig. 2.1, with its time-dependence in harmonic form, then electric filed **E** and magnetic field **H** can be represented as:

$$\mathbf{E} = \left[\mathbf{e_t}\mathbf{E_t}(r,\varphi) + \mathbf{e_z}E_z(r,\varphi)\right]e^{j(\omega t - \beta z)}, \tag{2.3a}$$

$$\mathbf{H} = \left[\mathbf{e_t}\mathbf{H_t}(r,\varphi) + \mathbf{e_z}H_z(r,\varphi)\right]e^{j(\omega t - \beta z)}, \tag{2.3b}$$

where β is the z-component of propagation vector, and it will be determined by boundary conditions later.

Before we substitute Eq. 2.3 into Eq. 2.2, it is worth noting that, the transverse components of **E** and **H** can be expressed in terms of E_z and H_z, based on the Maxwell's curl equations, together with the assumption that the form of time- and z- dependence follows $\sim e^{j(\omega t - \beta z)}$.

$$E_r = -\frac{j}{q^2}\left(\beta\frac{\partial E_z}{\partial r} + \frac{\mu\omega}{r}\frac{\partial H_z}{\partial \varphi}\right), \tag{2.4a}$$

$$H_r = \frac{j}{q^2}\left(\frac{\omega\varepsilon}{r}\frac{\partial E_z}{\partial \varphi} - \beta\frac{\partial H_z}{\partial r}\right), \tag{2.4b}$$

$$E_\varphi = \frac{j}{q^2}\left(\mu\omega\frac{\partial H_z}{\partial r} - \frac{\beta}{r}\frac{\partial E_z}{\partial \varphi}\right), \tag{2.4c}$$

$$H_\varphi = -\frac{j}{q^2}\left(\frac{\beta}{r}\frac{\partial H_z}{\partial \varphi} + \omega\varepsilon\frac{\partial E_z}{\partial r}\right), \qquad 2.4d$$

where

$$q^2 = \omega^2\varepsilon\mu - \beta^2 = k^2 - \beta^2 . \qquad 2.5$$

It is now explicit that, if one can find the solutions to E_z and H_z, one can determine the distribution of the entire electromagnetic field. Having this point been clarified, we substitute Eq. 2.3 into Eq. 2.2 in cylindrical coordinates, resulting in the *Helmholtz equation* for E_z and H_z,

$$\frac{\partial^2 E_z}{\partial r^2} + \frac{1}{r}\frac{\partial E_z}{\partial r} + \frac{1}{r^2}\frac{\partial^2 E_z}{\partial \varphi^2} + q^2 E_z = 0 , \qquad 2.6a$$

$$\frac{\partial^2 H_z}{\partial r^2} + \frac{1}{r}\frac{\partial H_z}{\partial r} + \frac{1}{r^2}\frac{\partial^2 H_z}{\partial \varphi^2} + q^2 H_z = 0 . \qquad 2.6b$$

Applying the approach of variable separation, we can obtain the solutions E_z and H_z as

$$E_z = \begin{cases} AJ_v(ur)e^{jv\varphi}e^{j(\omega t-\beta z)}, & |r| \le a \\ CK_v(wr)e^{jv\varphi}e^{j(\omega t-\beta z)}, & |r| > a \end{cases}, \qquad 2.7a$$

$$H_z = \begin{cases} BJ_v(ur)e^{jv\varphi}e^{j(\omega t-\beta z)}, & |r| \le a \\ DK_v(wr)e^{jv\varphi}e^{j(\omega t-\beta z)}, & |r| > a \end{cases}, \qquad 2.7b$$

where *A*, *B*, *C*, and *D* are arbitrary constants that are determined by the initial condition, and

$$u^2 = k_1^2 - \beta^2 , \qquad 2.8a$$

$$w^2 = \beta^2 - k_2^2 , \qquad 2.8b$$

which can be determined by the value of β.

To thoroughly determine E_z and H_z, the only unknown now is the propagation constant β. Yet we can only set the upper and lower boundaries of β from Eq. 2.8 as:

$$n_2\frac{2\pi}{\lambda} = k_2 \le \beta \le k_1 = n_1\frac{2\pi}{\lambda} , \qquad 2.9$$

but not all the values of β satisfying Eq. 2.9 can exist. A further constraint on β is the boundary conditions: The tangential components E_z, E_φ, H_z, and H_φ at the interface between the core and cladding should be respectively equal. In order to have E_φ and H_φ, we substitute Eq. 2.7 into Eqs. 2.4c and 2.4d and yields the form of E_φ and H_φ. Applying the boundary conditions to the corresponding components, we finally have the *characteristic equation* as below:

$$\left(\mathcal{J}_v+\mathcal{K}_v\right)\left(k_1^2\mathcal{J}_v+k_2^2\mathcal{K}_v\right)=\left(\frac{\beta v}{a}\right)^2\left(\frac{1}{u^2}+\frac{1}{w^2}\right)^2, \qquad 2.10$$

where $\mathcal{J}_v=\dfrac{J_v^{'}(ua)}{uJ_v(ua)}$, and $\mathcal{K}_v=\dfrac{K_v^{'}(wa)}{wK_v(wa)}$.

In practice, the refractive index difference is sufficiently small that makes $\Delta \ll 1$, and a simpler but highly accurate approximation, *weakly guiding fiber approximation*, can be performed on Eq. 2.10. When $\Delta \ll 1$, $n_1 \approx n_2$, Eq. 2.10 becomes

$$\frac{uJ_{j-1}(ua)}{J_j(ua)}=-\frac{wK_{j-1}(wa)}{K_j(wa)}. \qquad 2.11$$

The solutions to Eq. 2.11 are called *linearly polarized* (LP) modes. In Fig. 2.2, the intensity distributions of the first four LP modes are plotted.

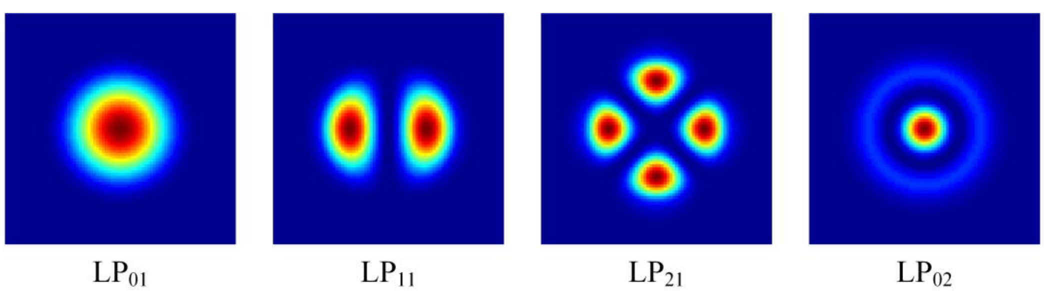

Fig. 2.2. Intensity profiles of the first four LP modes

2.1.2 Graded-Index Fibers and Mode Groups

Similar to the step-index fibers, the graded-index fibers are termed so due to the "graded" shape of their RI distribution along radius. One of the most common types of graded-index fibers possesses parabolic index profile along radius, defined as

$$n^2(r)=\begin{cases} n_1^2\left[1-2\Delta(r/a)^2\right], & |r|\le a \\ n_1^2\left[1-2\Delta\right]=n_2^2, & |r|>a \end{cases}, \qquad 2.12$$

where Δ is the refractive index difference, defined as:

$$\Delta=\frac{n_1^2-n_2^2}{2n_1^2}. \qquad 2.13$$

When the difference between n_1 and n_2 is on the order of 10^{-2}, the quantity Δ can be further simplified as:

$$\Delta\approx\frac{n_1-n_2}{n_1}. \qquad 2.14$$

Based on the assumption that the parabolic profile extends to infinity, one can solve the propagation constants β following similar steps when analyzing the step-index fibers [1]. We here skip all the derivations in [1] and directly to the conclusion: The propagation constant of the parabolic profile garded-index fiber can be represented as

$$\beta=n_1k\sqrt{1-4\Delta\frac{m}{V}}, \qquad 2.15$$

where $m=2\mu+v+1$ is the mode group number [2]. The mode group in graded-index fibers is essentially a group of LP modes that have the same $(2\mu+v+1)$ values, where μ denotes the azimuthal number, and v the radial number.

2.2 Wavefront Modulation

As we mentioned in the first chapter, the selective excitation of the desired modes are achieved through sophisticated input wavefront modulation, which can be performed primarily by SLMs and deformable mirrors (DMs).

2.2.1 Wavefront Modulation Process

The modulation process based on SLM is described mathematically in [3]. Here we consider the simplest case where we ignore all other linear optical components between the phase-only SLM and the fiber input end, as depicted in Fig. 2.3.

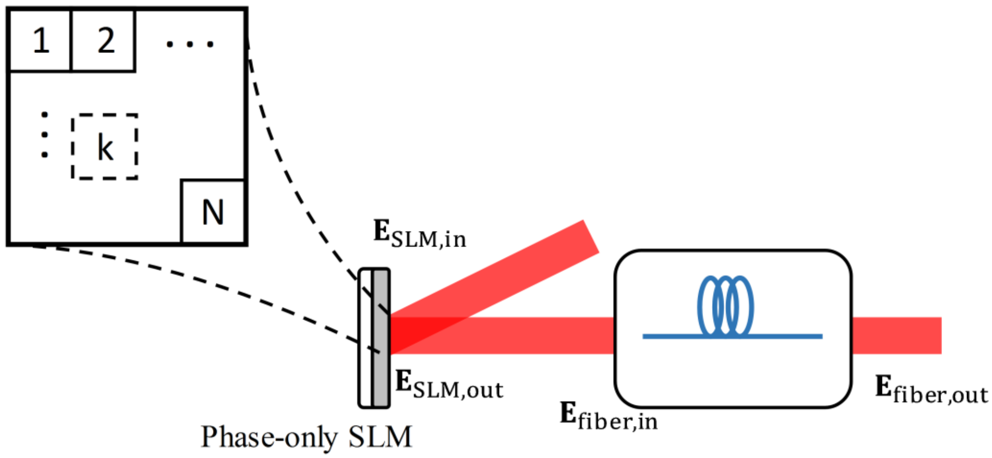

Fig. 2.3. Schematic of wavefront modulation based on phase-only SLM. SLM working area is divided into N identical blocks, which is shown as the illustration.

We define the complex reflectance of SLM as

$$V(x,y)=\sum_{k=1}^{N}\upsilon_k s_k(x,y)\,, \qquad 2.16$$

where υ_k denote the complex reflectance of the *k-th* block ($|\upsilon_k|=1$ for a phase-only SLM), *N* is the total number of blocks, and $s_k(x,y)$ is an indicator function of the *k-th* block:

$$s_k(x,y)=\begin{cases}1, & \text{if } (x,y) \text{ in the interior of the } k\text{-}th \text{ block}\\ 0, & \text{otherwise}\end{cases}.$$

After reflected by SLM, the field $\mathbf{E}_{\mathrm{SLM,out}}$ becomes:

$$\mathbf{E}_{\mathrm{SLM,out}}(x,y)=V(x,y)\mathbf{E}_{\mathrm{SLM,in}}(x,y)\,. \qquad 2.17$$

With the ignorance of all other linear optical components between the SLM and the fiber input end, the wave incident upon the fiber $\mathbf{E}_{\mathrm{fiber,in}}$ is supposed to be identical to the field reflected by the SLM, and thus we have

$$\mathbf{E}_{\text{fiber,in}}(x,y)=\mathbf{E}_{\text{SLM,out}}(x,y)=\sum_{k=1}^{N}\upsilon_k s_k(x,y)\mathbf{E}_{\text{SLM,in}}(x,y)=\sum_{k=1}^{N}\upsilon_k\mathbf{E}_{\text{k}}(x,y)\,, \tag{2.18}$$

where $\mathbf{E}_{\text{k}}$ corresponds to the portion of the electric field incident on the *k-th* block of the SLM.

Before we introduce any further systematic operations on $\mathbf{E}_{\text{fiber,in}}$, let's go back to the view of the optical fibers. According to the superposition theorem, any fields in an optical fiber can be represented as a linear combination of the fiber eigenmodes.

$$\mathbf{E}_{\text{fiber,in}}(x,y)=\sum_i c_i\mathbf{E}_{M,i}(x,y)+\text{radiation modes}\,, \tag{2.19}$$

where $\mathbf{E}_{M,i}$ is the *i-th* propagation mode supported by the fiber, and c_i the corresponding coefficient

$$\begin{aligned} c_i &= \iint\left[\mathbf{E}_{\text{fiber,in}}(x,y)\times\mathbf{H}^*_{M,i}(x,y)\right]\cdot\mathbf{e}_\mathbf{z}\,dxdy \\ &=\sum_{k=1}^{N} v_k\iint\left[\mathbf{E}_k(x,y)\times\mathbf{H}^*_{M,i}(x,y)\right]\cdot\mathbf{e}_\mathbf{z}\,dxdy \\ &=\mathbf{a}_i^T\boldsymbol{\upsilon}, \end{aligned} \tag{2.20}$$

$$a_{ik}=\iint\left[\mathbf{E}_k(x,y)\times\mathbf{H}^*_{M,i}(x,y)\right]\cdot\mathbf{e}_\mathbf{z}\,dxdy\,. \tag{2.21}$$

Physically, c_i quantifies the portion of the input field $\mathbf{E}_{\text{fiber,in}}$ that couples to the *i-th* propagation mode, and therefore one can describe the "coupling" of all propagating modes by a state vector $\mathbf{E}_{\text{coupled,in}}$ as

$$\mathbf{E}_{\text{coupled,in}}=\mathbf{c}=\mathbf{A}\boldsymbol{\upsilon}, \tag{2.22}$$

where

$$\mathbf{A}=\begin{pmatrix}\mathbf{a}_1^T\\ \mathbf{a}_2^T\\ \vdots\end{pmatrix}. \tag{2.23}$$

The optical signals should then experience phase-shifts and mode coupling during propagating within the fiber (for now we ignore all other potential phenomena), which can be described by a unitary operation **U**. After the propagation within the fiber, the electric field at the fiber output end can be represented by another state vector $\mathbf{E}_{\text{coupled,out}}$ as

$$\mathbf{E}_{\text{coupled,out}} = \mathbf{U}\mathbf{E}_{\text{coupled,in}} = \mathbf{U}\mathbf{A}\boldsymbol{\upsilon}\,. \qquad 2.24$$

Thus the electric field distribution at the fiber output end can be quantified as

$$\mathbf{E}_{\text{fiber,out}}(x,y) = \sum_i \mathbf{E}_{\text{coupled,out},i}\mathbf{E}_{M,i}(x,y) = \mathbf{M}^T(x,y)\mathbf{E}_{\text{coupled,out}}, \qquad 2.25$$

where

$$\mathbf{M}(x,y) = \begin{pmatrix} \mathbf{E}_{M,1}^T(x,y) \\ \mathbf{E}_{M,2}^T(x,y) \\ \vdots \end{pmatrix}. \qquad 2.26$$

Finally, the output electric field distribution can be represented as

$$\mathbf{E}_{\text{fiber,out}}(x,y) = \mathbf{M}^T(x,y)\mathbf{E}_{\text{coupled,out}} = \mathbf{M}^T(x,y)\mathbf{U}\mathbf{A}\boldsymbol{\upsilon} \propto \boldsymbol{\upsilon}, \qquad 2.27$$

which is a linear function of the SLM reflectance υ_k.

The linear dependence of output field distribution on SLM reflectance provides the theoretical support that, the output field distribution can be manipulate by the input wavefront modulation.

2.2.2 Mechanism of SLMs and DMs

In general, the phase modulation, *i.e.* the complex reflectance υ_i of SLM, can be represented as an additional exponential term multiplied by the original field,

$$\mathbf{E}_{\text{modulator,out}} = \mathbf{E}_{\text{modulator,in}}e^{j\phi}, \qquad 2.28$$

where $\phi = \frac{2\pi}{\lambda_0}nd$ denotes the phase shift introduced by modulators. Equation 2.28 reveals that the phase modulation could be achieved by varying either the refractive index n (SLMs) or optical path length d (DMs).

The most commonly used phase-only SLMs are based on untwisted nematic liquid crystal (NLC), the schematic is shown in Fig. 2.4. A thin layer of NLC is placed between two parallel transparent glass plates that are polished in the same direction shown in Fig. 2.4. In the absence of a steady electric field, the molecular direction is parallel to the direction of polish as illustrated in Fig. 2.4(a). When a steady field **E** is applied, as shown in Fig. 2.4(b), the molecules tend to align in the direction of the applied field, the equilibrium titled angle θ is quantified as

$$\theta = \begin{cases} 0, & \theta \le V_C \\ \dfrac{\pi}{2} - 2\tan^{-1}\exp\left(-\dfrac{V - V_C}{V_0}\right), & \theta > V_C \end{cases}, \tag{2.29}$$

where V_C is the threshold voltage for titling occurrence, and V_0 is a constant.

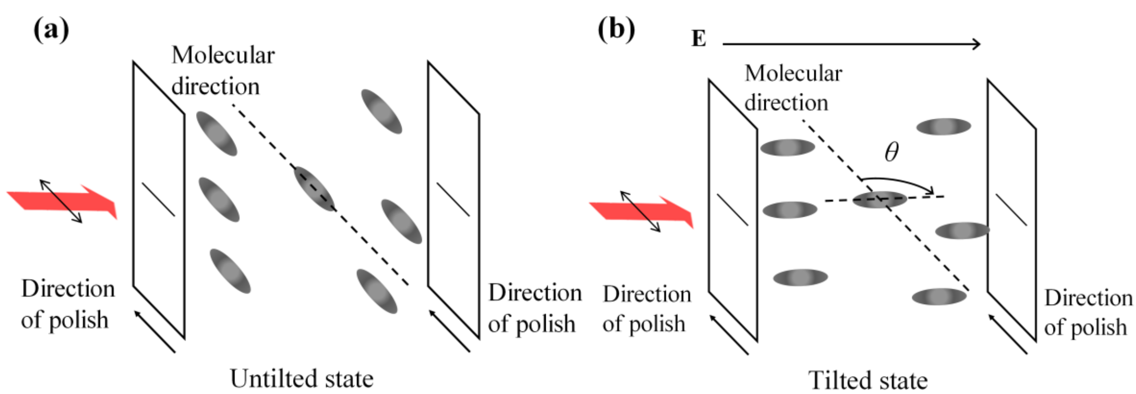

Fig. 2.4. (a) Untilted state in the absence of a steady electric field. (b) Tilted state when a steady electric field is applied.

A normal incident light with polarization in parallel with the polishing direction, will experience different effective indices with varied tilted angles. For a tilted angle θ, the effective index $n(\theta)$ is represented as [4]

$$\frac{1}{n^2(\theta)} = \frac{\cos^2\theta}{n_e^2} + \frac{\sin^2\theta}{n_o^2}. \tag{2.30}$$

Therefore, the untwisted NLC SLM can serve as a phase-only modulator for the lights with polarization parallel to the polishing direction. However, there are two major drawbacks of the NLC-based SLMs: Each device has a very limited working wavelength range, and the response time of the liquid crystal molecules to the applied electric field is relatively slow. These two issues can be adequately addressed when using DMs to manipulate the wavefront.

Briefly speaking, DMs use electrostatically induced mechanical deformation to modulate a reflected light wave. One of the most advanced DMs have been developed by *Boston Micromachines Corporation*, which consists of mirror membrane supported by an underlying actuator array, and each actuator in the array can be individually deflected by electrostatic actuation to achieve the desired pattern of deformation. The schematic is shown in Fig. 2.5(a). A negative bias voltage is applied to the metalized membrane, when a positive voltage is applied to the address electrodes under the membrane, the electrostatic forces force the membrane to move downward [5], as shown in Fig. 2.5(b). Furthermore, the moving distance can be determined individually in each actuator, by applying distinct positive voltages to individual address electrodes.

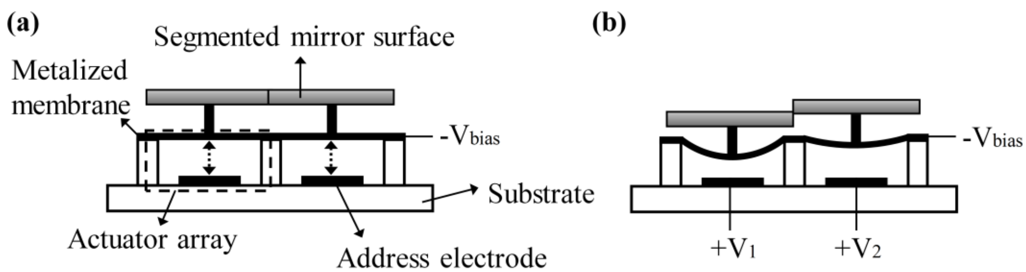

Fig. 2.5. Schematic of (a) segmented DM when no positive address voltage is applied, and (b) when different address voltages $+V_1$ and $+V_2$ are applied to individual address electrodes.

2.3 Fiber Bragg Gratings

The uniform Bragg grating inscribed in an optical fiber introduces a periodic dielectric perturbation along light propagation direction, which is shown in Fig. 2.6.

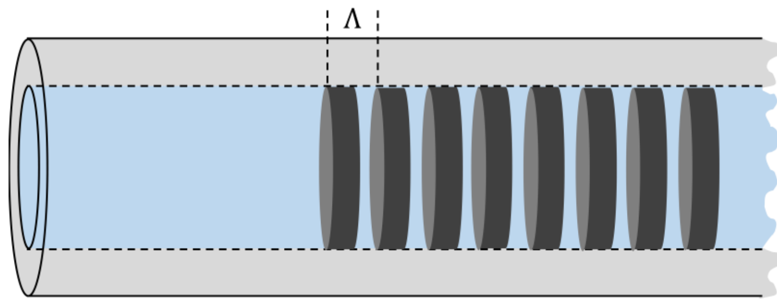

Fig. 2.6. Schematic of a uniform FBG with period Λ.

2.3.1 Fabrication

When exposing photosensitive fibers to ultraviolet (UV) light, we can induce a permanent refractive index change in the fiber core region, due to the photosensitivity of optical fibers. Photosensitivity may be regarded as quantification of the amount of fiber core index change following a specific UV light exposure [6]. Based on UV light exposure, there are three major approaches to inscribe Bragg gratings within optical fibers: Interferometric fabrication, phase mask, and point-by-point (PBP) techniques. Briefly speaking, interferometric technique is based on the interference pattern of two first-split-then-combined UV lights, the two light beams need to be focused to the fiber core where the interference occurs. Phase mask technique employs a diffractive optical element to spatially control the UV beam. PBP technique induces core index changes a step at a time, and thus possesses the highest flexibility to alter the Bragg grating parameters. More details can be found in [6].

2.3.2 Coupled-Mode Theory

The detailed derivation of coupled-mode theory [7] might be beyond the scope of this thesis, here we merely show the major conclusions.

In the presence of dielectric perturbation $\Delta\varepsilon$, wave equation Eq. 2.2a becomes

$$\left\{\nabla^2 + \omega^2\mu\left[\varepsilon_a\left(x,y\right) + \Delta\varepsilon(x,y,z)\right]\right\}\mathbf{E} = 0, \tag{2.31}$$

where ε_a is the unperturbed permittivity. Again, from the superposition theorem, the electric field $\mathbf{E}$ can be presented as a superposition of unperturbed waveguide eigenmodes

$$\mathbf{E}=\sum_m A_m(z)E_m\left(x,y\right)\exp\left[j(\omega t-\beta_m z)\right], \tag{2.32}$$

where the expansion coefficient $A_m(z)$ depends on *z*.

Further, since the perturbation $\Delta\varepsilon(x,y,z)$ is periodic in *z*, therefore we can expand it as a Fourier series

$$\Delta\varepsilon(x,y,z)=\sum_{m\neq 0}\varepsilon_m(x,y)\exp\left(-jm\frac{2\pi}{\Lambda}z\right), \tag{2.33}$$

Substitution of Eqs. 2.32 and 2.33 into Eq. 2.31, together with the assumption that the perturbation is “weak” yields

$$\frac{d}{dz}A_k=-j\frac{\beta_k}{\left|\beta_k\right|}\sum_m\sum_n C_{kn}^{(m)}A_n\left(z\right)\exp\left[j\left(\beta_k-\beta_n-\frac{m2\pi}{\Lambda}\right)z\right], \tag{2.34}$$

where $C_{kn}^{(m)}$ is the coupling coefficient, defined as

$$C_{kn}^{(m)}=\frac{\omega}{4}\int\mathbf{E}_k^*\cdot\varepsilon_m(x,y)\cdot\mathbf{E}_n\,dx\,dy, \tag{2.35}$$

which quantifies the coupling strength between the modes E_k and E_n introduced by ε_m.

It is worth noting from Eq. 2.34 that, a strong coupling occurs only when, firstly

$$\beta_k-\beta_n-\frac{m2\pi}{\Lambda}=0, \tag{2.36}$$

secondly,

$$C_{kn}^{(m)}\neq 0. \tag{2.37}$$

Eq. 2.36 is the *phase-matching condition*, which is simplified further for the uniform FBGs as

$$n_{\mathrm{eff,k}}+n_{\mathrm{eff,n}}=\frac{\lambda_0}{\Lambda}. \tag{2.38}$$

Equations 2.37 and 2.38 determines whether a strong coupling occurs between two counter-propagating waves, these two waves can either belong to the same fiber modes ($k = n$), or to adjacent fiber modes ($k \neq n$) [8].

References

1. Olshansky, R. "Propagation in glass optical waveguides." *Reviews of Modern Physics* 51.2 (1979): 341.
2. Streifer, William, and Clark N. Kurtz. "Scalar analysis of radially inhomogeneous guiding media." *JOSA* 57.6 (1967): 779-786.
3. Mahalati, Reza Nasiri, et al. "Adaptive control of input field to achieve desired output intensity profile in multimode fiber with random mode coupling." *Optics express* 20.13 (2012): 14321-14337.
4. Teich, Malvin Carl, and B. Saleh. *Fundamentals of photonics*. Canada, Wiley Interscience 3, 1991.
5. Goodman, Joseph W. *Introduction to Fourier optics*. Roberts and Company Publishers, 2005.
6. Kashyap, Raman. *Fiber bragg gratings*. Academic press, 2009.
7. Yariv, Amnon, and Pochi Yeh. *Photonics: optical electronics in modern communications*. Vol. 6. New York: Oxford University Press, 2007.
8. Mizunami, Toru, et al. "Bragg gratings in multimode and few-mode optical fibers." *Journal of lightwave technology* 18.2 (2000): 230.

Chapter 3

Adaptive Mode Control in Four- and Seventeen-Mode Fibers

3.1 Introduction

Recently, few-mode fibers (FMFs) have been studied for numerous potential applications including optical communications [1-3] and optical sensing [4-6]. Using mode-division-multiplexing (MDM) [7], for example, an FMF that supports M modes can increase the data transmission rate by a factor of M when each mode is used as a distinct communication channel. Additionally, since different linearly polarized (LP) modes propagating inside an FMF respond differently to the surrounding environment, FMF-based sensors can be used to simultaneously monitor multiple sensing parameters [8, 9].

A major challenge of using FMFs is the presence of intermodal coupling that can significantly increase the complexity of data processing [10]. Therefore, in order for such FMF-based applications to work effectively, reducing the impact of intermodal coupling and controlling the mode profile within an FMF are essential. Several methods have been reported in the literature to control mode profiles in FMFs [11-14]. In particular, we used feedback signals produced by optical intensity distribution [11], coupling ratio of a directional coupler [12], and optical reflection by an FBG [13, 14] to govern adaptive optics (AO) algorithm to control the form of optical waves in a two-mode fiber (TMF). Another example is reported in [15] to also control the mode profiles in a TMF using adaptive polarizers. However, the existing studies were only conducted using TMFs. In this work, we extend our method reported in [11] to excite a specific LP mode in four- and seventeen-mode fibers. The accuracy of selective modal excitation is evaluated through comparing the profiles of the experimentally produced LP modes with those calculated theoretically. Additionally, we report a nonlinear optimization algorithm which extracts the complex amplitudes of different LP modes using the intensity-based images and we apply it to decompose the experimentally obtained results for the four-mode fiber. The reported mode control method would address important problems found in high-order mode-division-multiplexers and optical sensors.

3.2 Methods

Our experimental setup is shown in Fig. 3.1. A single mode fiber coupled laser diode (QPhotonics, QFLD-660-10S) generates linearly polarized signal at 660 nm. The laser beam is collimated to pass through a half-wave plate followed by a polarizer. The light beam is then reflected by a mirror towards a phase-only spatial light modulator (SLM) (Holoeye, Pluto). The polarizer rotates light polarization to be in parallel with the optical table, which is in the same direction as modulation axis of the SLM, and the half-wave plate maximizes the light intensity accordingly. The center functional area of the SLM screen (approximately 6.2 mm by 6.2 mm) is divided into 9×9 identical square phase modulation blocks to modulate the expanded light wavefront. A 10× (NA = 0.25) and a 40× (NA = 0.65) objective lens are used to focus the light into fiber and then expand it out of the fiber, respectively. A CCD camera captures the output laser beam intensity profile, whose correlation with a target image is calculated by the computer (PC) and used as our feedback signal for mode control.

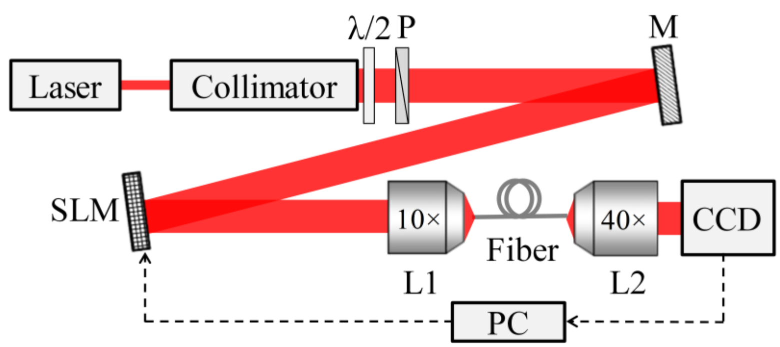

Fig. 3.1. Schematic of the experimental setup. λ/2: half-wave plate; P: polarizer; M: mirror; SLM: phase-only spatial light modulator; L1: 10× objective lens with NA = 0.25; L2: 40× objective lens with NA = 0.65; Fiber: ~ 1m; CCD: CCD camera.

We define an objective function *f(k)* which quantifies the correlation between the captured images and theoretical target images:

$$f(k) = 1 - \frac{\sum (I_0(x,y) - \overline{I}_0)(I_k(x,y) - \overline{I}_k)}{\sqrt{\sum (I_0(x,y) - \overline{I}_0)^2 \sum (I_k(x,y) - \overline{I}_k)^2}}, \qquad 3.1$$

where I_0 denotes the target intensity profile, and I_k represents what is captured by the CCD camera, $\overline{I_0}$ and $\overline{I_k}$ are the averaged I_0 and I_k, respectively. As Eq. 3.1 shows, a smaller *f(k)* indicates higher similarity between the captured and target images. Using the stepwise sequential algorithm [16], the phase of the individual blocks of the SLM is changed sequentially to reshape the beam profile at the output end of the FMF. This optimization process is repeated in cycles until $f(k)$ is minimized. The completion time of each optimization cycle is approximately 180 s and it is mainly dependent of the SLM speed. More details about this process can be found in [11].

3.3 Results

We first use a silica fiber (Thorlabs, SMF-28-J9) in our experimental setup. According to the specifications of this fiber, it supports four LP modes (six modes when mode-degeneracy is considered) at the operation wavelength. Starting with an arbitrary intensity profile, we adaptively reshape it to excite a specific LP mode at the fiber output end. The results of two representative experiments (Exp1 and Exp2) are shown in Fig. 3.2(a) and 3.2(b), respectively. In Fig. 3.2, each column corresponds to an independent optimization process to excite one of the LP modes at the fiber output; the first row represents the initial optical intensity profiles captured by the CCD camera, the second row shows the target images generated by theoretical analysis, and the third row reveals the optimized intensity profiles captured by the CCD camera after a completed optimization process. From the two sets of results, it is convincing to say that, at the fiber output, we can modulate a certain but arbitrary light intensity profile to any desired LP mode as long as it is supported by the fiber.

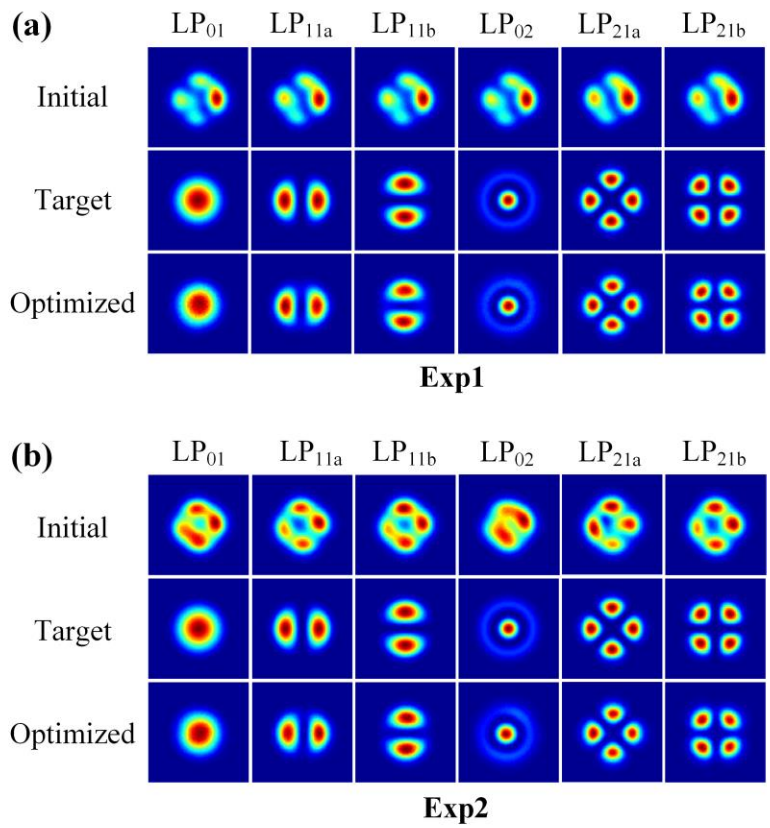

Fig. 3.2. Selective excitation of the individual LP modes in a four-mode fiber for (a) Exp1 and (b) Exp2.

Figure 3.3 illustrates the variations of the objective function *f(k)* with the optimization cycles for Exp1. Within each optimization cycle, *f(k)* exhibits significant variations. This is due to the fact that the SLM inevitably produces numerous "wrong" wavefronts before selecting the most appropriate one for the desired outcome. However, it is clear that the objective function tends to decrease consistently throughout the entire optimization process. Additionally, Fig. 3.3 suggests that it generally take 3 or 4 optimization cycles to achieve *f(k)* less than ~ –20 dB for all LP modes.

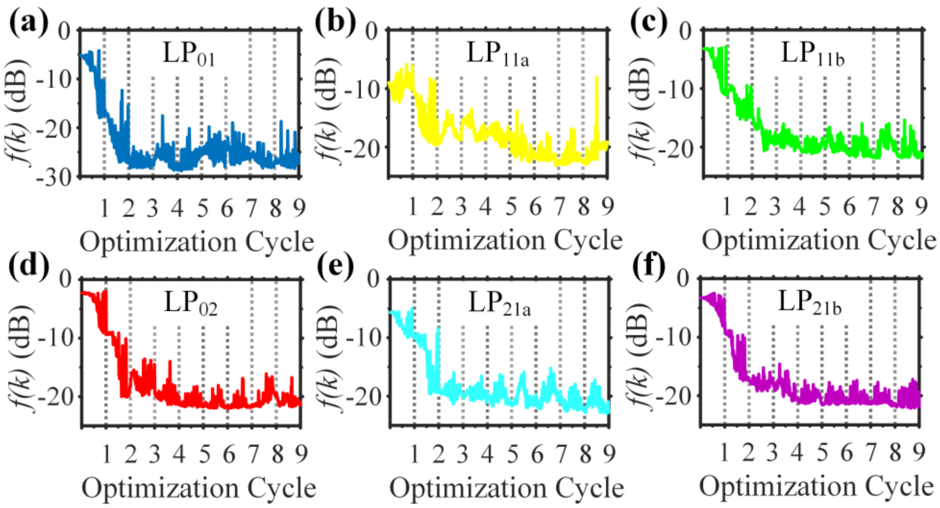

Fig. 3. Variations of the objective function *f(k)* obtained during the optimization process for Exp1 to excite the pure (a) LP_{01}, (b) LP_{11a}, (c) LP_{11b}, (d) LP_{02}, (e)LP_{21a} , and (f) LP_{21b} mode.

To further assess the accuracy of the mode control experiment, we compare in Fig. 3.4 the optimized intensity profiles (depicted in red square) within vertical cross-section with their corresponding theoretical targets (depicted in solid blue line). The illustrations in Figs. 4(a)-4(d) are for the optimized intensity profiles of Exp1 when exciting the LP_{01}, LP_{11b}, LP_{02} and LP_{21a} mode, respectively. The dashed line indicates the cross-section we chose. As can be seen, the optimized intensity profiles are consistent with the theoretical profiles.

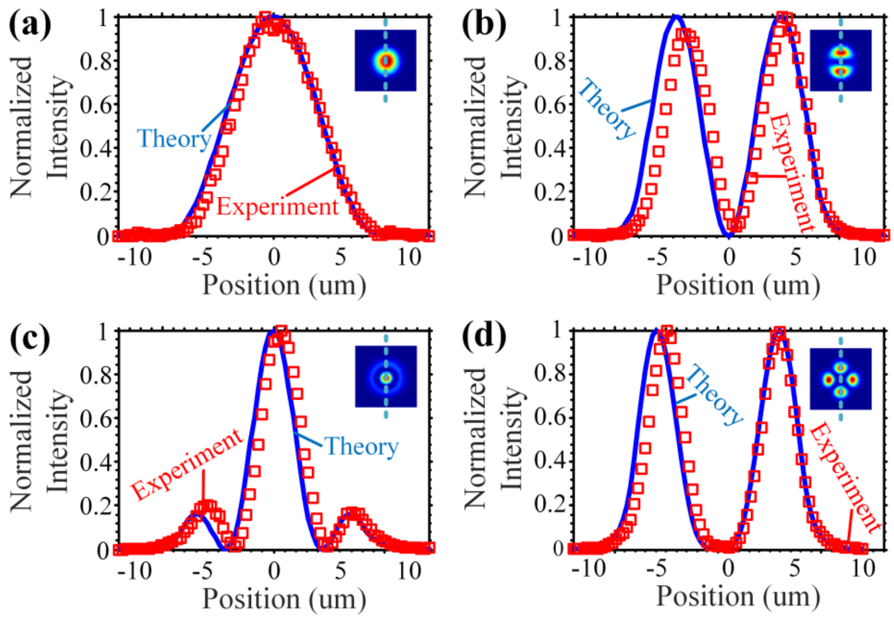

Fig. 3.4. Comparison of optimized intensity profiles (red square) and their corresponding theoretical distributions (blue solid line) within vertical cross-section when exiting the (a) LP_{01}, (b) LP_{11b}, (c) LP_{02} and (d) LP_{21a} mode in Exp1.

In order to evaluate the ratio of the power of an optimized LP mode to the total power of all modes, we introduce a mode-decomposition algorithm based on nonlinear optimization. Here, we express optical intensity distribution within the four-mode fiber as:

$$I(x,y) = \left| \sum_{lm} A_{lm} \exp(j\theta_{lm}) \vec{E}_{lm}(x,y) \right|^2, \quad 3.2$$

where $\vec{E}_{lm}(x,y)$ and $A_{lm}\exp(j\theta_{lm})$ are the field distribution and the complex amplitude of an LP_{lm} mode, respectively. Without loss of generality, we normalize the amplitudes and the phases of all LP modes relative to that of the LP_{01} mode. As a result, we can define the vector **X** that includes the values of the complex amplitudes of different modes as:

$$\mathbf{X} = \left[1 \;\; A_{11a}\exp(j\theta_{11a}) \;\; A_{11b}\exp(j\theta_{11b}) \;\; \cdots \;\; A_{21b}\exp(j\theta_{21b})\right]. \quad 3.3$$

Furthermore we equalize $\iint \left|\vec{E}_{lm}(x,y)\right|^2 dxdy$ of all LP modes to unity. Our goal is to reconstruct the vector **X** that minimizes the objective function *f*(*k*), defined in Eq. 3.1, to increase the correlation between the CCD camera image ($I^{CCD}(x,y)$), and the "reconstructed" image ($I^{R}(x,y)$)

calculated using the reconstructed mode coefficient $\mathbf{X^R}$. The reconstruction algorithm is illustrated in Fig. 3.5(a). To start reconstruction, we first capture the to be decomposed CCD camera image of intensity distribution $I^{CCD}(x,y)$. Then, to expedite our optimization problem, we normalize the maximum of $I^{CCD}(x,y)$ to unity to get $I_N^{CCD}(x,y)$, where the subscript "*N*" denotes "normalization". Afterwards, we randomly choose an initial guess for $\mathbf{X}$ and denote it as $\mathbf{X^1}$. Substituting with $\mathbf{X^1}$ into Eq. 3.2 and, again to expedite the optimization problem, normalizing its maximum to unity, we calculate $I_N^1(x,y)$. Normalization of the CCD camera image $I_N^{CCD}(x,y)$ and the reconstructed intensity distribution $I_N^1(x,y)$ is optional. Doing so, however, can significantly speed up the nonlinear optimization process. We then substitute $I_N^{CCD}(x,y)$ and $I_N^1(x,y)$ into Eq. 3.1 to calculate the objective function *f*. The goal of the nonlinear optimization process is to minimize the value of the objective function as much as possible. If, after the first run, the value of *f* is not minimized, we use an interior-point programming algorithm [17], implemented through the Matlab "fmincon" function (Mathworks, 2013), to update the trial solution from $\mathbf{X^1}$ to $\mathbf{X^2}$. This process continues until the convergence criterion is met. We denote the final reconstructed amplitude-phase vector as $\mathbf{X^R}$. The only constraint applied in this nonlinear optimization method is any amplitude in the $\mathbf{X^R}$ belongs to the interval [0,100]. Practically, this interval is sufficient to represent any combinations of LP modes or even a pure one. To avoid the nonlinear optimization process being stuck at a local minimum, we perform the optimization process in parallel starting at ten different initial random vectors, which we find can guarantee obtaining the correct global solution. Figure 3.5(b) shows representative results of applying the reported nonlinear optimization algorithm. The left column includes three arbitrary captured CCD camera images, and the right column shows their corresponding reconstructed images. The high similarity between the original and reconstructed images confirms the ability to reconstruct the amplitude-phase vector with high accuracy.

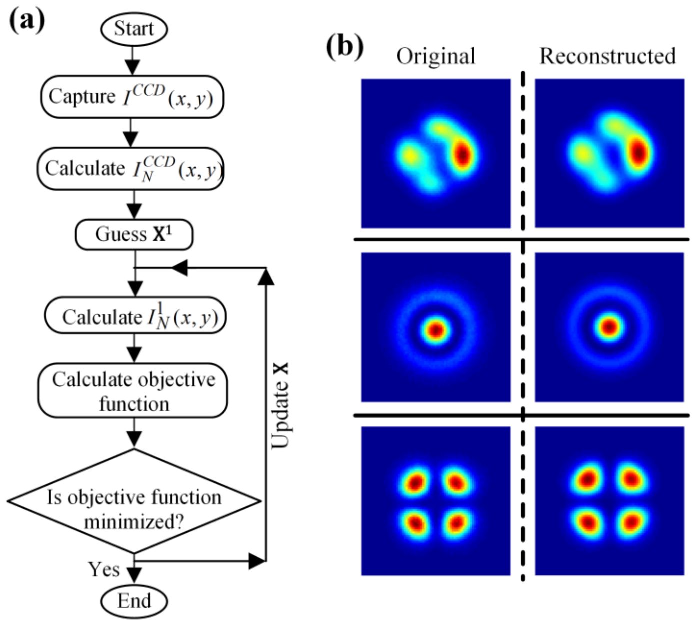

Fig. 3.5. (a) Flowchart of the nonlinear optimization process for mode-decomposition. (b) Original and reconstructed intensity profiles for three representative experiments.

We then apply this nonlinear optimization process for the CCD camera images captured after each optimization cycle when exciting the different six LP modes. We define the purity of any given LP_{lm} mode purity as the ratio of its power to the total power, *i.e.* $|A_{lm}|^2/\sum_{lm}|A_{lm}|^2$. Figure 3.6 shows the purity of the target LP modes during Exp1 after each optimization cycle. The mode purity that can be obtained after finishing the whole mode control experiment is approximately between 85% and 97%.

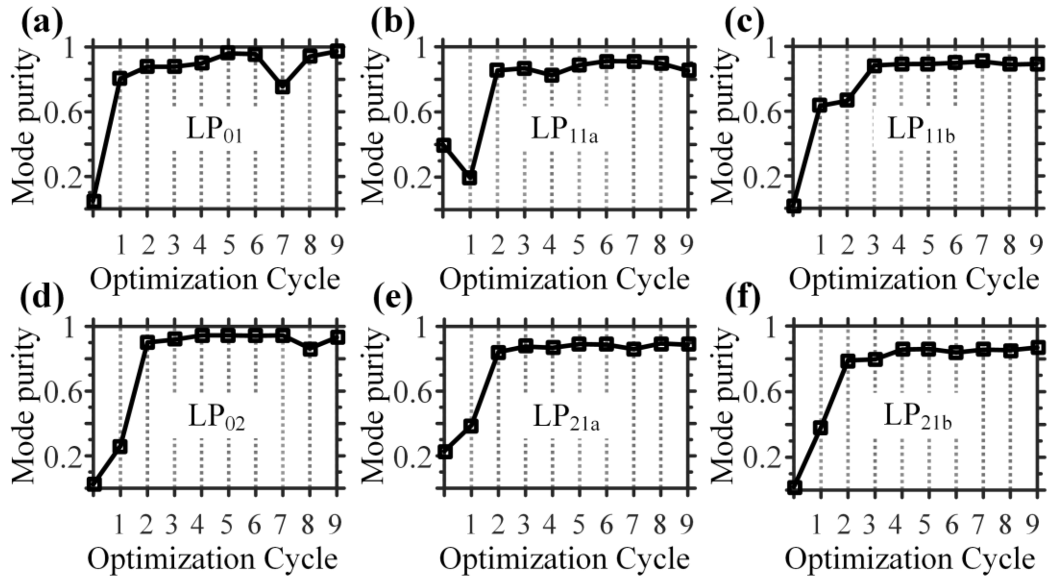

Fig. 3.6. Mode purity of the (a) LP_{01}, (b) LP_{11a}, (c) LP_{11b}, (d) LP_{02}, (e) LP_{21a} and (f) LP_{21b} mode after each optimization cycle during Exp1.

The same experimental procedure can also achieve selective LP mode excitation in a seventeen-mode fiber (Optical Fiber Solutions 60816, operated at 660 nm). (If counting degenerate LP modes as distinct, the fiber supports 28 modes.) Representative experimental results are shown in Fig. 3.7 where we select the LP_{03}, LP_{13a}, LP_{42a}, and LP_{61a} as our target modes.

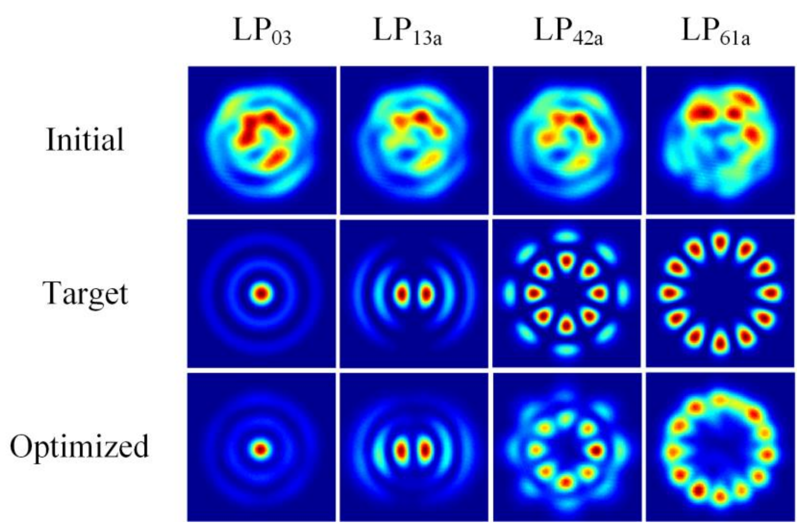

Fig. 3.7. Selective excitation of the individual LP_{03}, LP_{13a}, LP_{42a}, and LP_{61a} mode in the seventeen-mode fiber.

Figure 3.8 plots the objective functions *f(k)* for the optimization processes shown in Fig. 3.7. The objective functions in this case saturate at higher values than those of the four-mode fiber experiments. This is to be expected since, as the number of LP modes supported by an FMF increases, intermodal coupling, which is caused by fiber bending, stress, etc. [18], becomes more effective. Consequently, because of inevitable mechanical vibrations, the modes transfer matrix might slightly change during the mode optimization experiment which causes deviation from getting the optimum target. However, these results are still very beneficial for applications not contingent on exciting exactly pure LP modes. For example, in a quasi-distributed FMF-absorption-based optical sensing network [5], a beam of light intensity focused around the fiber axis is used for signal delivery and collection, and another beam distributed around the core-cladding interface is utilized for absorption-based sensing. Additionally, the mode control in the seventeen-mode fiber could be improved by reducing the time of the optimization experiment via using faster adaptive light wavefront modulator, such as deformable mirror [13], instead of the SLM we use.

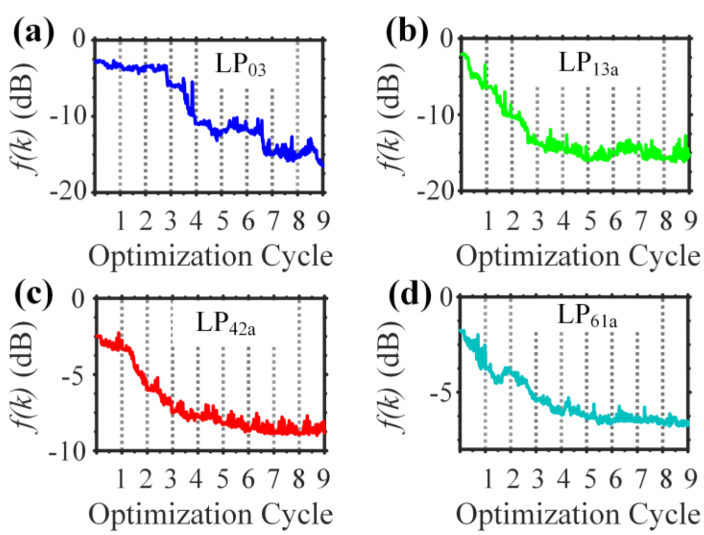

Fig. 3.8. Variations of the objective function *f(k)* obtained during the optimization process to excite the purely (a) LP_{03}, (b) LP_{13a}, (c) LP_{42a} and (d) LP_{61a} mode in the seventeen-mode fiber.

In Fig. 3.9, we show the horizontal cross-section of the profiles of the optimized modes shown in Fig. 7, and their corresponding theoretical ones. Comparing the results shown in Fig. 3.4 and Fig.

3.9, we again confirm that the less the number of LP modes supported by an FMF, the higher mode selectivity for the mode control experiment.

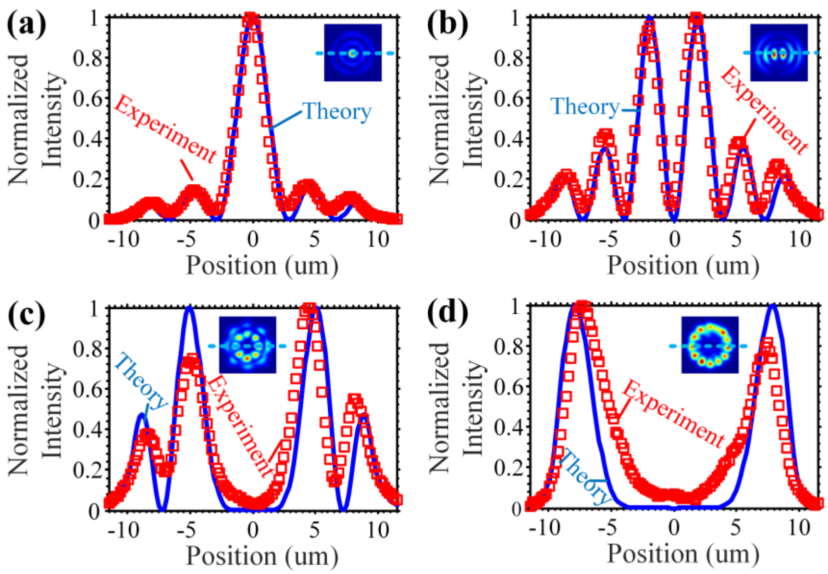

Fig. 3.9. Comparisons of optimized Intensity profiles (red square) and their corresponding theoretical distributions (blue solid line) within horizontal cross-section when exiting the (a) $LP_{03,}$ (b) LP_{13a}, (c) LP_{42a} and (d) LP_{61a} mode.

Finally, the aforementioned mode decomposition algorithm cannot be applied for the case of the seventeen-mode fiber. This is because, for the seventeen-mode fiber, the number of the unknowns in the **X** vector is relatively large (54 amplitude and phase values) which makes the reverse nonlinear optimization problem ill-posed. However, another image-based mode decomposition technique [19] might be helpful to solve this large scale inverse problem.

3.4 Future Applications

The obtained results would have potential applications in both optical communications and sensing. For example, an optimized LP mode at the end of an FMF could be injected to another identical FMF using 4f system [20] to design a mode-division multiplexer. Furthermore, controlling the distribution of the optical power within the fiber to be around the core-cladding interface (higher order modes excitation) or to be concentrated around the fiber-axis (lower order modes excitation) is important to design large scale absorption-based sensing networks with high sensitivity as in [5].

References

1. C. Koebele, M. Salsi, D. Sperti, P. Tran, P. Brindel, H. Mardoyan, S. Bigo, A. Boutin, F. Verluise, P. Sillard, M. Astruc, L. Provost, F. Cerou, and G. Charlet, "Two mode transmission at 2x100Gb/s, over 40km-long prototype few-mode fiber, using LCOS-based programmable mode multiplexer and demultiplexer," Opt. Express **19**, 16593-16600 (2011).
2. A. Li, A. Al Amin, X. Chen, and W. Shieh, "Reception of Mode and Polarization Multiplexed 107-Gb/s CO-OFDM Signal over a Two-Mode Fiber," 2011 Optical Fiber Communication Conference and Exposition (OFC/NFOEC) and the National Fiber Optic Engineers Conference (2011).
3. R. Ryf, S. Randel, A. H. Gnauck, C. Bolle, A. Sierra, S. Mumtaz, M. Esmaeelpour, E. C. Burrows, R. J. Essiambre, P. J. Winzer, D. W. Peckham, A. H. McCurdy, and R. Lingle, "Mode-Division Multiplexing Over 96 km of Few-Mode Fiber Using Coherent 6 x 6 MIMO Processing," J. Lightwave Technol. **30**, 521-531 (2012).
4. A. Kumar, N. K. Goel, and R. K. Varshney, "Studies on a few-mode fiber-optic strain sensor based on LP01-LP02 mode interference," J. Lightwave Technol. **19**, 358-362 (2001).
5. I. Ashry, A. B. Wang, and Y. Xu, "Mode-division-multiplexing of absorption-based fiber optical sensors," Opt. Express **24**, 5186-5202 (2016).
6. I. Ashry, A. B. Wang, and Y. Xu, "Mode-Based Reconstruction of Chemical Distributions in Optical Fibers," IEEE J. Sel. Top. Quantum Electron. **23** (2017).
7. S. Berdague and P. Facq, "Mode Division Multiplexing in Optical Fibers," Appl. Opt. **21**, 1950-1955 (1982).
8. A. Li, Y. F. Wang, and W. Shieh, "Few-mode Fiber Based Optical Sensors," IEEE Photon. Conf. (2015).
9. C. L. Zhao, X. F. Yang, M. S. Demokan, and W. Jin, "Simultaneous temperature and refractive index measurements using a 3 degrees slanted multimode fiber Bragg grating," J. Lightwave Technol. **24**, 879-883 (2006).
10. S. O. Arik, D. Askarov, and J. M. Kahn, "Effect of Mode Coupling on Signal Processing Complexity in Mode-Division Multiplexing," J. Lightwave Technol. **31**, 423-431 (2013).
11. P. Lu, M. Shipton, A. B. Wang, S. Soker, and Y. Xu, "Adaptive control of waveguide modes in a two-mode-fiber," Opt. Express **22**, 2955-2964 (2014).

12. P. Lu, M. Shipton, A. B. Wang, and Y. Xu, "Adaptive control of waveguide modes using a directional coupler," Opt. Express **22**, 20000-20007 (2014).
13. P. Lu, A. B. Wang, S. Soker, and Y. Xu, "Adaptive mode control based on a fiber Bragg grating," Opt. Lett. **40**, 3488-3491 (2015).
14. P. Lu, I. Ashry, and Y. Xu, "Adaptive Mode Control for Few-Mode Fiber Based Sensors and Sensor Networks," J. Lightwave Technol. **35**, 3562-3568 (2017).
15. L. J. Huang, J. Y. Leng, P. Zhou, S. F. Guo, H. B. Lu, and X. A. Cheng, "Adaptive mode control of a few-mode fiber by real-time mode decomposition," Opt. Express **23**, 28082-28090 (2015).
16. I. M. Vellekoop and A. P. Mosk, "Phase control algorithms for focusing light through turbid media," Opt. Commun. **281**, 3071-3080 (2008).
17. A. Wachter and L. T. Biegler, "On the implementation of an interior-point filter line-search algorithm for large-scale nonlinear programming," Math. Prog. **106**, 25-57 (2006).
18. L. Palmieri, "Coupling mechanism in multimode fibers," Next-Generation Optical Communication: Components, Sub-Systems, and Systems Iii **9009** (2014).
19. L. J. Huang, S. F. Guo, J. Y. Leng, H. B. Lu, P. Zhou, and X. Cheng, "Real-time mode decomposition for few-mode fiber based on numerical method," Opt. Express **23**, 4620-4629 (2015).
20. G. Stepniak, L. Maksymiuk, and J. Siuzdak, "Increasing Multimode Fiber Transmission Capacity by Mode Selective Spatial Light Phase Modulation," 2010 36th European Conference and Exhibition on Optical Communication (ECOC), Vols 1 and 2 (2010).

Chapter 4

Adaptive Mode Control in Highly Multimode Fibers

4.1 Introduction

In the last decade, we have witnessed an exponential increase of the studies on multimode fibers (MMFs), for their potential applications in optical communications [1-3], sensing [4], imaging [5, 6], and micromanipulation [7] to name a few. However, practical expansions of such applications are always limited by the MMF nature that gives rise to modal dispersion [2], together with inevitable modal chaos introduced by imperfect fabrication, fiber bending, stress, etc. [8]. These two factors twist together to render the MMF an unpredictable and unreliable signal transmission channel [9]. It is thus strongly desired to determine and further control light propagation within MMFs.

To date, multiple approaches have been reported to control wave propagation in MMFs through the fiber input field modulation. In general, these existing approaches can be divided into two major categories. The first one modulates the fiber input wavefront based on prior knowledge of the MMF transfer matrix (TM) calculated by either empirical measurement [5] or numerical modeling [9]. However, for most practical applications, accurate measuring or estimating the TM can be very difficult and may require frequent MMF calibrations. The other class of controlling wave propagation in MMFs is based on adaptive optics (AO) [10, 11]. The AO feedback is provided by calculating the correlation between a desired mode profile at the fiber output end and the actual captured one. Then, the input field is manipulated in a way to maximize the correlation. The AO-based approach does not require prior knowledge of the optical system, and is inherently tolerant of environmental perturbations. Such features can compensate the complexity and unpredictability of light propagation within MMFs, thus making AO suitable for a wide range of practical applications. In general, existing methods of wavefront control in MMFs can only selectively excite a desired mode profile only at *the output end* of an MMF, and not *within* it. The only exception is the case when the MMF TM is calculated through numerical modeling, however, its usage is limited to step-index MMFs of just few centimeters length [9]. For optical imaging related applications, for example, one is mainly concerned with the optical intensity distribution at the MMF output port [5]. But if we extend the concept of controlling the mode profiles for MMF-based optical sensing applications, it is essential to be able to control the form of optical fields within the MMF at a sensing segment. The reason is that the response of an MMF-based sensor can be highly mode dependent. For example, in an MMF-absorption-based sensor [12], higher-order modes of light intensity focused at the core-cladding interface offer higher absorption attenuation than the lower-order ones concentrated around the fiber axis.

In this work, we extend our method introduced in [13, 14] to use AO with feedback from a fiber Bragg grating (FBG) written in an MMF to selectively excite principal modes *within* the MMF and at the FBG location. A principal mode in an MMF is a group of multiple linearly polarized (LP) modes that have identical propagation constants [15, 16]. The FBG can naturally distinguish these principal modes by assigning each mode a unique Bragg wavelength calculated using the phase-matching condition [16].

4.2 Methods

We firstly characterize the reflection spectrum of the FBG which provides feedback signal during our adaptive mode control experiment. The FBG reflection spectrum is measured using the setup in Fig. 4.1(a) which includes a component test system (CTS, Micron Optics, HR-SLI), a circulator, and a standard Bragg grating (Ascentta Inc.) written in a graded-index MMF (~1.2 m, Corning ClearCurve OM2). As shown in Fig. 4.1(a), the three ports of the circulator are made of single mode fiber (SMF) and connected/spliced to the CTS/MMF. Since SMF delivers only the fundamental LP_{01} mode to the MMF, we intentionally bend the MMF to excite as many core modes as possible within it. A representative FBG reflection spectrum is shown in Fig. 4.1(b). Each dominant reflection peak, located by a solid grey line, corresponds to a Bragg wavelength (λ_B) of an individual principal mode. The Bragg wavelengths of various principal modes are shifted because each of them has a unique effective refractive index [16]. Because of intermodal coupling, the mixed principal modes create tiny peaks in the FBG reflection spectrum, as those identified by the dashed grey lines in Fig. 4.1(b). The measured spectrum is in general consistent with the results in [16], except for some missing reflection peaks in the shorter wavelength range. We attribute such missing to splicing the MMF to the SMF which, even with bending the MMF, does not necessarily guarantee exciting higher-order modes which possess shorter Bragg wavelengths.

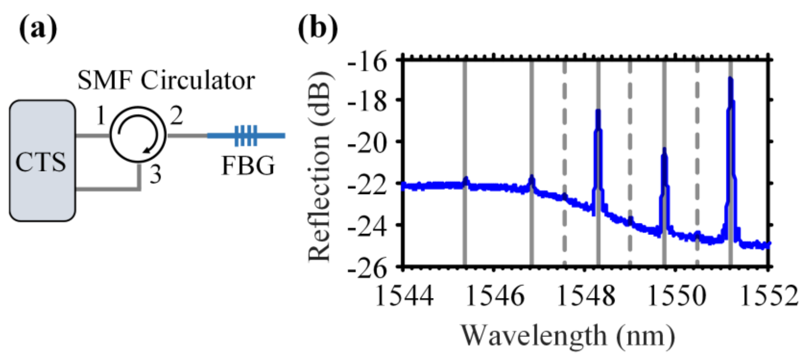

Fig. 4.1. (a) Experimental setup for measuring the FBG reflection spectrum. The FBG is written in an MMF (blue line) while all other components are connected using SMFs (grey line). (b) Representative reflection spectrum of the FBG. The Bragg wavelengths of the individual principal modes and the mixtures of adjacent principal modes are located by the solid and dashed grey lines, respectively.

After characterizing the reflection spectrum of the FBG, we can then carry out the mode control experiment using the setup shown in Fig. 4.2. A tunable laser (New Focus, TLB-6728) is used to generate a continuous wave light at a predetermined wavelength (one of the measured Bragg wavelengths of the principal modes). The laser beam is then coupled into free space through a collimator (L1). The wavefront of the collimated beam is modulated by a deformable mirror (DM) (Boston Micromachines) which consists of 140 blocks. Afterwards, the modulated beam is focused by an objective lens (L2, 10×) into the MMF with the FBG written near its output port. At the output of the MMF, an objective lens (L3, 100×) is used to collimate the transmitted beam which is then split by a beam splitter (BS1). One of the split beams is captured by an infrared CCD (Hamamatsu, C10633-13), and the power of the identical other one is measured using a photodiode (PD1). Since the FBG is placed near the MMF output, we can use the CCD images to validate the results of the mode control at the FBG location. Before L2, a beam splitter (BS2) is placed to collect the reflected beams from the MMF, either Fresnel or FBG reflections. The reflected power is measured by a photodiode (PD2). Signals from the PD1 and PD2 are acquired by a digitizer (National Instruments, NI-5114, 250 MS/s sampling rate), and analyzed by the computer (PC) to provide the feedback for the DM for adaptive mode control.

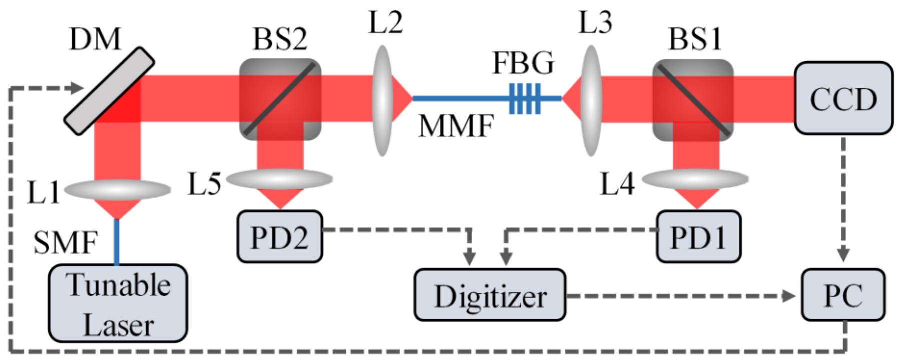

Fig. 4.2. Experimental setup for FBG-based adaptive mode control within an MMF. L1, collimator, NA=0.24; L2 and L5, 10× objective lens, NA=0.25; L3, 100× objective lens, NA=0.9; L4, 20× objective lens, NA=0.4.

Our adaptive mode control is based on the algorithm described in [13] which requires identifying a feedback function (F) as:

$$F = \frac{P_R - P_{BG}}{P_T} \propto \frac{V_{PD2} - V_{BG}}{V_{PD1}}, \qquad 4.1$$

where P_R denotes the total reflected power, P_T is the transmitted power, and P_{BG} represents the background power reflected by all other optical components, including fiber facets, except the FBG. Experimentally, it is easier to write Eq. 4.1 in terms of the voltages measured by PD1 and PD2. In other words, V_{PD2} and V_{BG} are the voltages measured by PD2 when receiving P_R and P_{BG}, respectively. Similarly, V_{PD1} is the voltage recorded by PD1 when receiving P_T. In order to experimentally measure V_{BG}, we fix the laser power and tune the operation wavelength away from the Bragg wavelengths range. Under this scenario, the measured V_{PD2} equals V_{BG}.

Having defined the feedback function in Eq. 4.1, we can then explain the principle of our algorithm for principal mode control in MMF. Suppose we tune the operation wavelength to one of the Bragg wavelengths identified in Fig. 4.1(b) by solid grey lines. At this Bragg wavelength, several principal modes can ideally be excited at the location of the FBG. However, only one of them, which satisfies the Bragg condition at the operation wavelength, is reflected back by the FBG. If such a principal mode dominates the incident wave at the FBG location, it experiences a strong reflection and a weak transmission, which leads to a large F value. Consequently, when the operation wavelength matches one of the Bragg wavelengths, maximizing the feedback function

F results in exciting a single pure principal mode at the FBG location. Experimentally, *F* is maximized through programming the DM to adaptively modulate the wavefront of the incident light beam. We identically set the 140 blocks of the DM to individually produce 12 different phase shift values between 0 and ~2π. As we previously reported in [13], for each block, the 12 phase shifts are sequentially applied. We then record the phase shift value for each block which maximizes *F*. Afterwards, we simultaneously apply the recorded 140 phase shifts of the individual block to complete one optimization cycle. Starting from the obtained optimized phase shifts, we then initiate a new optimization cycle. The optimization cycles are repeated until the *F* value almost saturates at a maximum value. For a more detailed description on the algorithm and the optimization procedure, refer to [13].

4.3 Results

Following the optimization algorithm described above, we can start with an arbitrary intensity profile at the FBG location and adaptively reshape it until it turns to the desired principal mode. We carry out three representative experiments (Exp1-Exp3) to respectively excite a low-, an intermediate-, and a high-order mode group at the FBG location. In Exp1-Exp3, we respectively set the operation wavelength to 1551.25 nm, 1546.69 nm, and 1540.56 nm to match the Bragg wavelengths of the desired principal modes. Figs. 3(a)-3(c) show the initial (labeled as “Init.”) and the optimized (labeled as “Opt.”) intensity distributions of Exp1-Exp3, respectively. For clarification, the “Init.” intensity distributions are those captured by the CCD camera before running the optimization experiment, while the “Opt.” ones are the final images after finishing the optimization cycles. In each experiment (Exp1-Exp3), we carry out four independent optimization trials (Trial1-Trial4), such that the initial intensity distribution at the FBG location in each trial is different. We intentionally select two of the initial intensity distributions to be concentrated around the MMF axis and the other two are quite scattered within the MMF core. Eventually, each trial (Trial1-Trial4) is repeated three times (Run1-Run3) to test the repeatability of our results. As shown in Fig. 4.3(a), regardless of the initial intensity distribution, the optimized ones are always concentrated around the fiber axis. In contrast, as observed in Figs. 4.3(b) and 4.3(c), the intensity centralization around the MMF axis of the optimized principal modes decreases as their order increases. These results agree with theoretical expectations in terms of the correlation between the order of a principal mode and its spatial intensity distribution. It is worth noticing that, in each experiment (Exp1-Exp3), the optimized profiles are different, likely due to the fact that a principal mode contains multiple LP modes with similar propagation constants but significantly different optical field distributions. As a result, the optimization process may end up exciting a random superposition of LP modes that belong to the same principal mode. Even if we start with the same initial intensity distribution, as shown in Run1-Run3 in Fig. 4.3, the inevitable slight mechanical vibrations which occur during the mode optimization process may drift the final superposition weights of the LP modes of the optimized principal mode, and thus the final profile differs at each run. Similar results were obtained in [13] when we adaptively tried to excite the LP_{11} mode at a FBG location within a two-mode fiber. In such case, the optimized profiles were always random superpositions of the two degenerate LP_{11a} and LP_{11b} modes.

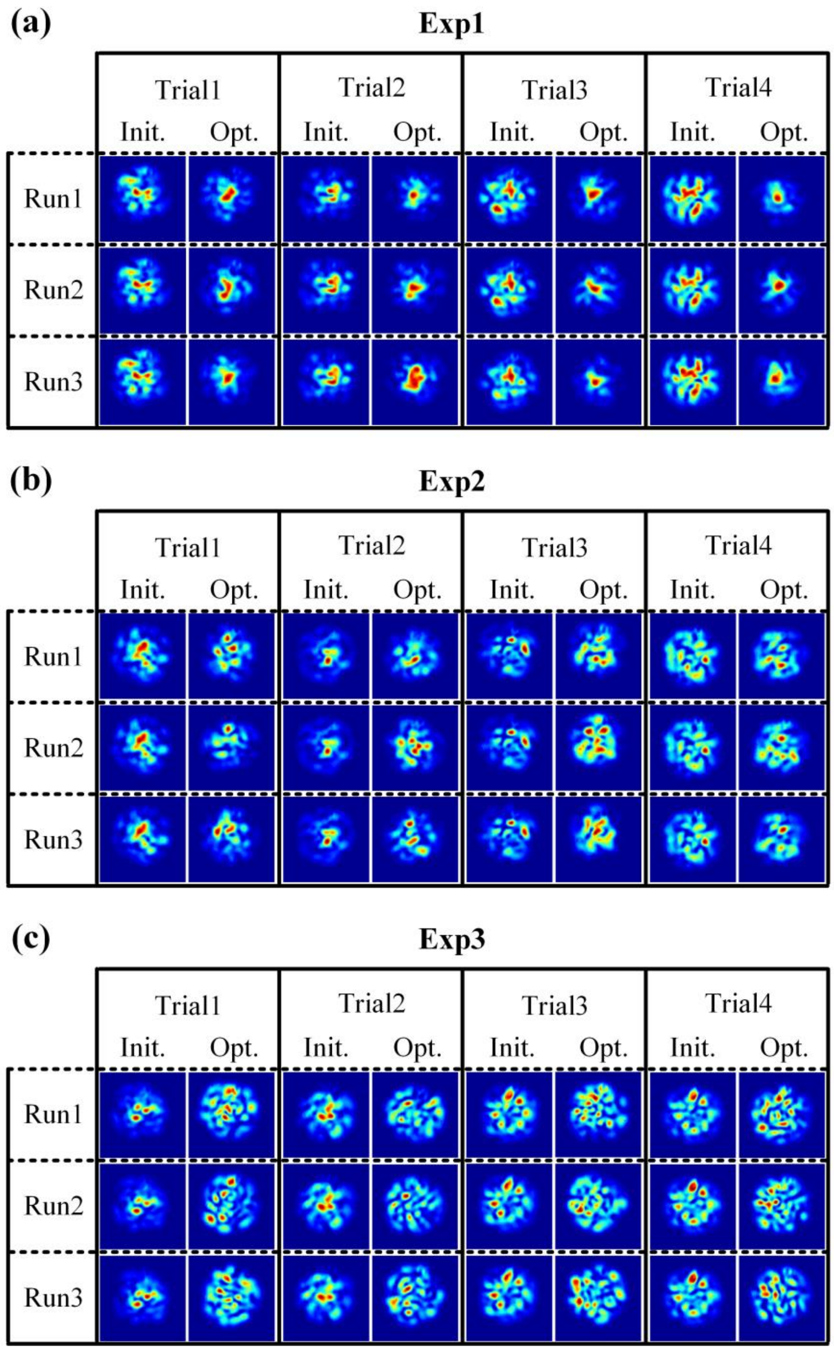

Fig. 4.3. Representative experimental results when exciting (a) a low-, (b) an intermediate-, and (c) a high-order principal mode at the FBG location. In each subfigure, the solid black lines separate the four different trials, and the dashed black lines set apart the three independent runs repeated for the same initial intensity distribution.

In order to prove that the optimized mode profiles obtained in each experiment (Exp1-Exp3) all belong to the same desired principal mode, we carry out the following verification process. In each of Exp1-Exp3, right after every complete optimization run, we apply the optimized phase shift values of the 140 DM blocks which results in exciting the optimized mode profile at the FBG location. Then, we tune the operation wavelength (λ) within ± 0.4 nm away from the Bragg wavelength at which we carry out the optimization experiment. While tuning the operation wavelength, using Eq. 4.1, we calculate $F(\lambda)$ every 0.1 nm step. Using the CCD camera, we experimentally observe a slight change in the optimized profile as we tune the operation wavelength. This change increases with raising the difference between the operation wavelength and the Bragg wavelength of the optimized principal mode. To make sure that the change in FBG reflection is not caused by the change in mode composition, we choose the ± 0.4 nm wavelength tuning range to ensure that the overall optical intensity distribution at the fiber output remains similar within this tuning range. This is quantified by defining a normalized correlation function ρ_N as:

$$\rho_N = \frac{\sum (I_\lambda(x,y) - \bar{I}_\lambda)(I_{\lambda_B}(x,y) - \bar{I}_{\lambda_B})}{\sqrt{\sum (I_\lambda(x,y) - \bar{I}_\lambda)^2 \sum (I_{\lambda_B}(x,y) - \bar{I}_{\lambda_B})^2}}, \qquad 4.2$$

where I_λ and I_{λ_B} are the CCD intensity profiles of the optimized mode captured at the shifted wavelength and its Bragg wavelength, respectively. The average of I_λ and I_{λ_B} are respectively denoted as $\bar{I}_\lambda$ and $\bar{I}_{\lambda_B}$. The summations in Eq. 4.2 cover the total number of pixels within an image captured by the CCD camera. Figures 4(a) and 4(b) show two representative examples for the change of ρ_N with ($\lambda - \lambda_B$), along with the corresponding CCD camera images captured after each wavelength tuning step for the optimized mode profiles of Exp1-Trial3-Run3 and Exp3-Trial3-Run3, respectively. As observed in these figures, ρ_N is within [0.9, 1] which indicates that the weights of the LP modes which belong to the optimized principal mode group remain almost constants when tuning the wavelength to calculate $F(\lambda)$ for the verification purpose. Figures 4.4(c)-4.4(e) show some representative examples for $[F(\lambda)/F(\lambda_B)]$ calculated for the optimized mode profiles obtained after Trial1 and Trial3 of Exp1-Exp3, respectively. As can be observed, in each experiment (Exp1-Exp3), the final optimized mode profiles possess the maximum $F(\lambda)$ value at the Bragg wavelengths at which we run the optimization processes, and smaller F values at the neighboring wavelengths. In other words, based on the definition of F in Eq. 4.1, all of the optimized mode profiles obtained during each of Exp1-Exp3 experience maximum reflection and minimum transmission when passing through the FBG at the experiment Bragg wavelength, compared to the neighboring wavelengths. Combining this result with that of the intensity distributions of the optimized mode profiles with respect to the MMF axis, one can conclude that all of the target mode profiles obtained in each experiment (Exp1-Exp3) belong to the same desired principal mode.

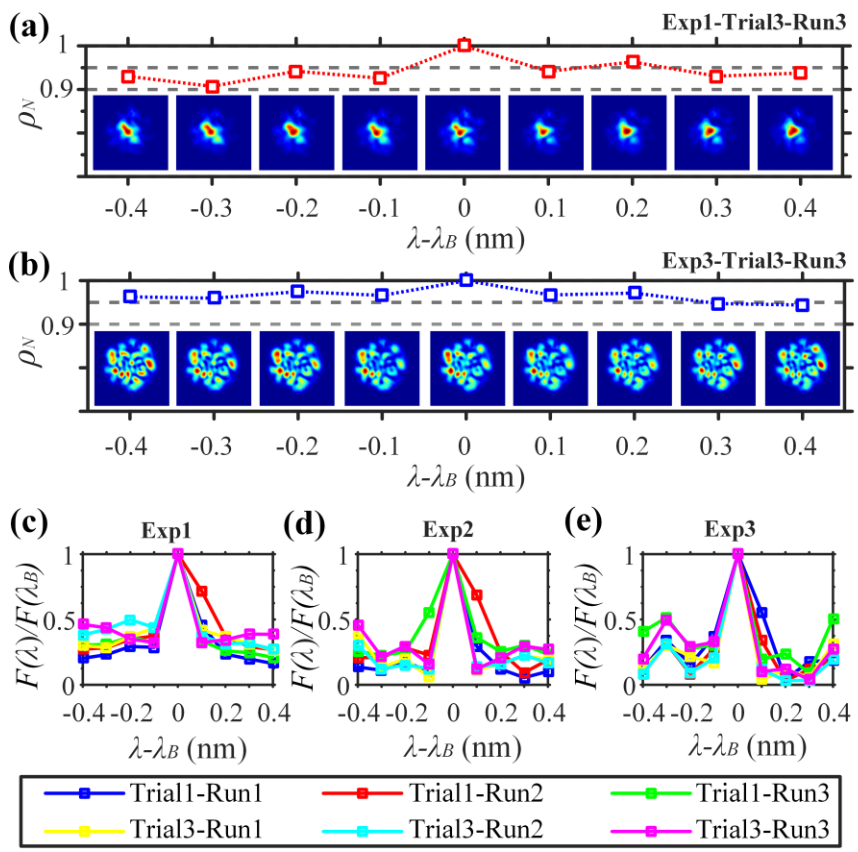

Fig. 4.4. Normalized correlation ρ_N between the optimized mode profiles captured at the shifted wavelengths and the one at the Bragg wavelength, calculated after (a) Exp1-Trial3-Run3, and (b) Exp3-Trial3-Run3. Change of the feedback function with the wavelength shift from the Bragg wavelength of (c) Exp1, (d) Exp2, and (e) Exp3. For each experiment (Exp1-Exp3), all three runs (Run1-Run3) of Trial1 and Trial3 are presented and denoted as "Trail1-Run1", "Trial1-Run2", etc. in different colors.

To take a deeper view into the optimization process, in Figs. 4.5(a)-4.5(c), we show the variations of the feedback function F during the entire optimization process (nine cycles in total) of six representative runs. The selected six examples are Run1 of Trial1 and Trial3 in each experiment (Exp1-Exp3) which intentionally include focused and scattered initial intensity distributions. Within each optimization cycle, F values experience significant variations. This is because, following the optimization algorithm, the DM inevitably excites numerous incorrect principal modes at the FBG location before getting the desired one. However, the general trend is clear: Throughout the entire optimization process, the feedback function tends to consistently increase until its average almost saturates around a maximum value. In Figs. 4.5(d) and 4.5(e), we show an example for the MMF output at the end of each optimization cycle obtained during Exp1-Trial1-Run1 and Exp1-Trial3-Run1, respectively. Figs. 4.5(a)-4.5(e) together suggest that it usually takes less than 6 optimization cycles for an arbitrary profile to become the desired principal mode.

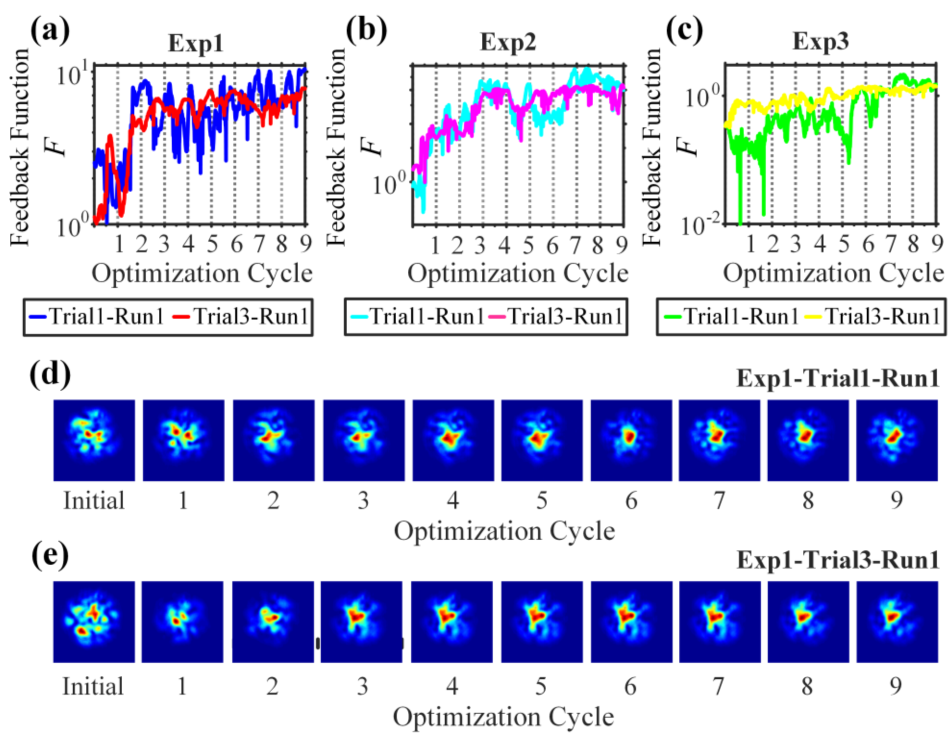

Fig. 4.5. Variations of the feedback function F during the 9 optimization cycles of Trial1-Run1 and Trial3-Run1 in (a) Exp1, (b) Exp2, and (c) Exp3. The initial intensity distributions and the optimized ones at the end of each optimization cycle obtained during (d) Exp1-Trial1-Run1, and (e) Exp1-Trial3-Run1, respectively.

4.4 Future Applications

It is worth mentioning that we fail to apply this AO method to control principal modes within relatively long MMF (~>50 m). This is because the modes transfer matrix of the long MMF rapidly changes relative to the time of the optimization experiment. However, our results are still very beneficial for the short-distance MMF-based applications, such as the case in some optical imaging [6, 17] and sensing [18, 19] systems.

References

1. H. R. Stuart, "Dispersive multiplexing in multimode optical fiber," Science **289**, 281-283 (2000).
2. A. R. Shah, R. C. J. Hsu, A. Tarighat, A. H. Sayed, and B. Jalali, "Coherent optical MIMO (COMIMO)," J. Lightwave Technol. **23**, 2410-2419 (2005).
3. B. Franz and H. Bulow, "Experimental Evaluation of Principal Mode Groups as High-Speed Transmission Channels in Spatial Multiplex Systems," IEEE Photon. Technol. Lett. **24**, 1363-1365 (2012).
4. E. B. Li, X. L. Wang, and C. Zhang, "Fiber-optic temperature sensor based on interference of selective higher-order modes," Appl. Phys. Lett. **89** (2006).
5. T. Cizmar and K. Dholakia, "Exploiting multimode waveguides for pure fibre-based imaging," Nat. Commun. **3** (2012).
6. Y. Choi, C. Yoon, M. Kim, T. D. Yang, C. Fang-Yen, R. R. Dasari, K. J. Lee, and W. Choi, "Scanner-Free and Wide-Field Endoscopic Imaging by Using a Single Multimode Optical Fiber," Phys. Rev. Lett. **109** (2012).
7. T. Cizmar, M. Mazilu, and K. Dholakia, "In situ wavefront correction and its application to micromanipulation," Nat. Photonics **4**, 388-394 (2010).
8. L. Palmieri, "Coupling mechanism in multimode fibers," Next-Generation Optical Communication: Components, Sub-Systems, and Systems Iii **9009** (2014).
9. M. Ploschner, T. Tyc, and T. Cizmar, "Seeing through chaos in multimode fibres," Nat. Photonics **9**, 529-+ (2015).
10. I. M. Vellekoop and A. P. Mosk, "Phase control algorithms for focusing light through turbid media," Opt. Commun. **281**, 3071-3080 (2008).

11. R. N. Mahalati, D. Askarov, J. P. Wilde, and J. M. Kahn, "Adaptive control of input field to achieve desired output intensity profile in multimode fiber with random mode coupling," Opt. Express **20**, 14321-14337 (2012).
12. I. Ashry, A. B. Wang, and Y. Xu, "Mode-division-multiplexing of absorption-based fiber optical sensors," Opt. Express **24**, 5186-5202 (2016).
13. P. Lu, A. B. Wang, S. Soker, and Y. Xu, "Adaptive mode control based on a fiber Bragg grating," Opt. Lett. **40**, 3488-3491 (2015).
14. P. Lu, I. Ashry, and Y. Xu, "Adaptive Mode Control for Few-Mode Fiber Based Sensors and Sensor Networks," J. Lightwave Technol. **35**, 3562-3568 (2017).
15. R. Olshansky, "Propagation in Glass Optical-Waveguides," Rev. Mod. Phys. **51**, 341-367 (1979).
16. T. Mizunami, T. V. Djambova, T. Niiho, and S. Gupta, "Bragg gratings in multimode and few-mode optical fibers," J. Lightwave Technol. **18**, 230-235 (2000).
17. I. N. Papadopoulos, S. Farahi, C. Moser, and D. Psaltis, "Focusing and scanning light through a multimode optical fiber using digital phase conjugation," Opt. Express **20**, 10583-10590 (2012).
18. Y. H. Luo, B. B. Yan, M. Li, X. L. Zhang, W. X. Wu, Q. J. Zhang, and G. D. Peng, "Analysis of multimode POF gratings in stress and strain sensing applications," Opt. Fiber Technol. **17**, 201-209 (2011).
19. A. Sun and Z. S. Wu, "Multimode Interference in Single Mode-Multimode FBG for Simultaneous Measurement of Strain and Bending," IEEE Sensors J. **15**, 3390-3394 (2015).

Chapter 5

Conclusions

In this chapter, we summarize the experiment results presented in this thesis.

By using the correlation between the CCD camera image and the theoretical target profile as the feedback for SLM control, we experimentally demonstrate the feasibility and effectiveness of using AO to achieve highly selective mode excitations in four- and seventeen-mode fibers. The accuracy of our results is evaluated through calculating the normalized correlation between the optimized LP mode profiles and their corresponding theoretical ones. Furthermore, using nonlinear optimization, we report a mode decomposition algorithm which confirms the ability to excite an LP mode in the four-mode fiber with purity approximately between 85% and 97%.

By using AO with feedback as the FBG reflection/transmission ratio, we can adaptively excite a specific principal mode group within an MMF. We experimentally demonstrate that, by maximizing the feedback function F at the Bragg wavelength associated with a principal mode, we can selectively excite this principal mode group at the FBG location. This AO approach is applied at multiple Bragg wavelengths to individually excite low-, intermediate-, and high-order principal mode groups. The accuracy of our results is assessed through comparing the intensity distributions, with respect to the MMF axis, of the optimized mode profiles. For further verification, we also show that $F(\lambda)$ of an optimized principal mode has a maximum value only at its Bragg wavelength.